Journal of Vertebrate Paleontology

ISSN: (Print) (Online) Journal homepage: www.tandfonline.com/journals/ujvp20

New pterosaur remains from the Late Cretaceous of Afro-Arabia provide insight into flight capacity of large pterosaurs

Kierstin L. Rosenbach, Danielle M. Goodvin, Mohammed G. Albshysh, Hassan A. Azzam, Ahmad A. Smadi, Hakam A. Mustafa, Iyad S. A. Zalmout & Jeffrey A. Wilson Mantilla

To cite this article: Kierstin L. Rosenbach, Danielle M. Goodvin, Mohammed G. Albshysh, Hassan A. Azzam, Ahmad A. Smadi, Hakam A. Mustafa, Iyad S. A. Zalmout & Jeffrey A. Wilson Mantilla (05 Sep 2024): New pterosaur remains from the Late Cretaceous of Afro-Arabia provide insight into flight capacity of large pterosaurs, Journal of Vertebrate Paleontology, DOI: 10.1080/02724634.2024.2385068

To link to this article: https://doi.org/10.1080/02724634.2024.2385068

Published online: 05 Sep 2024.

Journal of Vertebrate Paleontology e2385068 (23 pages)

DOI: 10.1080/02724634.2024.2385068

ARTICLE

NEW PTEROSAUR REMAINS FROM THE LATE CRETACEOUS OF AFRO-ARABIA PROVIDE INSIGHT INTO FLIGHT CAPACITY OF LARGE PTEROSAURS

KIERSTIN L. ROSENBACH,[1] DANIELLE M. GOODVIN,[1] MOHAMMED G. ALBSHYSH,[2] HASSAN A. AZZAM,[3] AHMAD A. SMADI,[4] HAKAM A. MUSTAFA,[5] IYAD S. A. ZALMOUT, [1,6] and JEFFREY A. WILSON MANTILLA [1*]
[1]University of Michigan Museum of Paleontology and Department of Earth and Environmental Sciences, Ann Arbor, Michigan 48109-1085, U.S.A., klrose@umich.edu, goodvin@umich.edu, zalmouti@umich.edu, wilsonja@umich.edu;
[2]Madaba, 17110, Jordan, malbshysh80@gmail.com;
[3]Amman, 26110, Jordan, waelazzam2006@yahoo.com;
[4]Department of Earth Sciences, King Abdulaziz University, Jeddah, Saudi Arabia, smadijor1@gmail.com;
[5]Department of Earth and Environmental Sciences, Faculty of Science, Yarmouk University, Irbid, 211-63, Jordan, haksawalha@yahoo.com;
[6]Saudi Geological Survey, Sedimentary Rocks and Palaeontology Department, Jeddah, 11451, Saudi Arabia, izalmout@ksu.edu.sa

ABSTRACT—Pterosaurs were the earliest and largest vertebrates to evolve powered flight, but they are the only major volant group that has gone extinct. Attempts to understand pterosaur flight mechanics have relied on aerodynamic principles and analogy with extant birds and bats. Both lines of inquiry rely on the size, three-dimensional shape, and internal structure of flight bones, which in pterosaurs are surprisingly rare. Remarkably, two new large-bodied pterosaur individuals with three-dimensionally preserved wing elements were recently recovered from Upper Cretaceous (Maastrichtian) horizons of Jordan. Both specimens represent azhdarchoid pterosaurs; one is referrable to the giant species *Arambourgiania philadelphiae* (ca. 10 m wingspan) and the second to a new, smaller species *Inabtanin alarabia* gen. et sp. nov. (ca. 5 m wingspan). In this study, we describe these new specimens and use high-resolution micro-computed tomography scans to reconstruct and compare the internal osteology of the humeri of these two differently sized species to that of extant birds, for which internal bone structure can be correlated with flight behavior. The humerus of *Arambourgiania* exhibits a series of helical ridges formed along the cortical bone, whereas *Inabtanin* exhibits a denser pattern of hollow struts. Variation in internal structure for these individuals likely reflects responses to mechanical forces applied on the wings of pterosaurs. Results indicate that *Inabtanin* has internal bone morphology similar to that of flapping birds, whereas the internal morphology of *Arambourgiania* is most similar to that of soaring birds.

http://zoobank.org/urn:lsid:zoobank.org:pub:1C722D5A-CDBF-4E41-91A8-52CDC4B29349

Citation for this article: Rosenbach, K. L., Goodvin, D. M., Albshysh, M. G., Azzam, H. A., Smadi, A. A., Mustafa, H. A., Zalmout, I. S. A., & Wilson Mantilla, J. A. (2024) New pterosaur remains from the Late Cretaceous of Afro-Arabia provide insight into flight capacity of large pterosaurs. *Journal of Vertebrate Paleontology*. https://doi.org/10.1080/02724634.2024.2385068

Submitted: August 14, 2023
Revisions received: July 9, 2024
Accepted: July 18, 2024

INTRODUCTION

Pterosaurs are a group of extinct flying reptiles that existed from the Late Triassic to the Cretaceous–Paleogene extinction event. Pterosaurs evolved powered flight approximately 50 million years before flight feathers appeared in the fossil record, and some achieved wingspans twice that of the largest volant birds (12 vs. 6 m). Pterosaurs are notable for their patagium-based wings supported by elongated, pneumatic forelimbs. Their skeletons are characterized by a high degree of skeletal pneumaticity that exceeds that of all other archosaurs (Martin & Palmer, 2014a).

Postcranial skeletal pneumaticity actively remodels bone and accommodates the respiratory system in the form of air sacs. This adaptation both allows for a greater volume of air storage and reduces bone weight, both of which are advantageous to flying vertebrates. Postcranial skeletal pneumaticity is present in birds and inferred to have been present in pterosaurs based on the structure of their trabecular bone (Bonde & Christiansen, 2003; Britt, 1993; Butler et al., 2009; Claessens et al., 2009). Analysis of the internal bone structure of modern Aves suggests that remodeling of bone is a response to the stresses of flight and indicates that these distinct structures correlate with different flight styles (Novitskaya et al., 2017). Because these structures are diagnostic for flight style in birds, we hope to infer flight style in pterosaurs by identifying these patterns of pneumaticity in their limb bones. Although advantageous in life, postcranial pneumaticity renders pterosaur wing bones less resistant to post-mortem compressive forces, and as a result three-dimensional preservation is quite rare.

Recent fieldwork conducted by University of Michigan (UM) and the Natural Resources Authority of Jordan (NRA) in Upper Cretaceous deposits of Jordan uncovered two new pterosaur

*Corresponding author.
Color versions of one or more of the figures in the article can be found online at www.tandfonline.com/ujvp.

Published online 05 Sep 2024

specimens buried in environments that allowed for infilling of bone by limestone matrix and preservation of detailed three-dimensional structure (Figs. 1–2). Prior to these discoveries, the Maastrichtian vertebrate fossil record of Jordan consisted of isolated pterosaur specimens attributed to *Arambourgiania philadelphiae* (Arambourg, 1959; Frey & Martill, 1996; Martill & Moser, 2017), one of the largest known azhdarchid species. These specimens were recovered from the phosphate mines of Ruseifa, near the Jordanian capital of Amman. Prospection in the area uncovered the shaft of an exceptionally large humerus attributed to *Arambourgiania* (estimated wingspan 10 m). In addition, exposures of the Muwaqqar Formation in south-central Jordan yielded a partial pterosaur skeleton (estimated wingspan 5 m) from a site near Tal Inab. Its distinct spatiotemporal context, large body size, and long, edentulous beak suggest that it represents a new azhdarchoid species. Here we describe these specimens, discuss their internal bone structure, and infer flight capacity and flight style in these two large pterosaurs.

METHODS

We scanned individual skeletal elements in a micro-computed tomography (μCT) scanner at the Computed Tomography Laboratory at the Department of Earth and Environmental Sciences, which is equipped with a Nikon XT H 225 ST. We mounted specimens vertically along their longest axis, supported by floral foam inside a cardboard tube affixed to a 15 cm-thick cardboard base. We autoconditioned the scanner to maximum capacity at 225 kV to accommodate long scans of fossils with a matrix that has a similar density to bone. The scanner is equipped with a tungsten target. Scan voltage ranged from 175–205 kV and current ranged from 200–255 μA, depending upon the element. We set exposure times between 1.42 and 2.83 seconds. To maintain the grayscale histogram values at a minimum near 10,000 and maximum near 60,000, we used copper filters ranging in width from 1.5–2.5 mm. Each scan had a resolution between 50–60 microns. For elements that were too large to scan at this resolution, we completed multiple overlapping scans of smaller regions. For each scan, we chose to enable flux normalization, capture 2 frames per projection, and minimize ring artifacts. With these settings, scans typically took 12 hours to complete. We reconstructed the resulting scans using CT Pro 3D and saved the reconstructions as volume files.

We processed the volume files using Mimics image processing software (Materialize NV) to visualize the CT slices for segmentation. We then proceeded through the CT slices in intervals from the proximal to distal end of each humerus to capture internal structures using the segmenting tools *Lasso*, *LiveWire*, *Mask*, and *Interpolate*. For each CT slice, one of us (DMG) selected all trabecular bone to add to the *Mask*, which differentiated the trabecular bone from the matrix. A completely segmented slice displays black air space, gray matrix, and highlighted bone. After each slice was segmented, we scrolled distally and repeated the process on a subsequent slice. In regions where the struts had a dense distribution or complex internal structure, we segmented slice-wise to minimize interpolation. In regions where the trabecular bone was sparse or simple and elongate, we segmented approximately every 10 slices. Once a bone was completely segmented, we used the *Interpolate* tool, which connects consecutive segmented structures to produce a 3D model that accurately reconstructs the true anatomy. The resulting 3D model allows us to explore the image and categorize the internal bone structure according to structures present (struts or ridges). Finally, we oriented these models vertically along their long axes and used the *Angles* tool to measure the angles of individual struts or ridges in relation to the long axis of the wing bone and in relation to intersecting trabecular bone. CT data are available from University of Michigan Deep Blue Data (https://doi.org/10.7302/c1fs-xb12).

Institutional Abbreviations—**AMNH**, American Museum of Natural History, New York, U.S.A.; **NRA**, Natural Resources Authority of Jordan, Amman, Jordan; **SNSB-BSPG**, Staatliche Naturwissenschaftliche Sammlungen Bayerns–Bayerische Staatssammlung für Paläontologie und Geologie, Munich, Germany; **UJA**, University of Jordan, Amman, Jordan; **UMMP**, University of Michigan Museum of Paleontology, Ann Arbor, U.S.A.; **YUPC**, Yarmouk University Paleontological Collection in the Department of Earth and Environmental Sciences, Irbid, Jordan.

SYSTEMATIC PALEONTOLOGY

PTEROSAURIA Kaup, 1834
PTERODACTYLOIDEA Plieninger, 1901
AZHDARCHOIDEA Nesov, 1984
INABTANIN ALARABIA, gen. et sp. nov.
(Figs. 2–11)

Holotype—A partial skeleton of an adult individual consisting of an upper and lower jaw, three cervical vertebrae and a small fragment of a fourth, a left scapulocoracoid, a left humerus, and a nearly complete right wing consisting of a humerus, radius, ulna, metacarpal IV, and first wing phalanx (YUPC-INAB-6-001–010).

Horizon and Locality—The specimen was collected at locality Inab-6, located 34 km north of the current border with Saudi Arabia (Fig. 1). Stratigraphic information was collected by the authors in collaboration with the NRA (Fig. 1b). Field reports record 12 units fining upwards. These units consist of alternating clays, limestones, chalks, and phosphates. *Inabtanin* was found in situ in a ca. 70 cm-thick layer of gray limestone containing reddish-gray lenses and occasional bands of fibrous gypsum (up to 6-10 cm thick). The Inab section is consistent with the paleoenvironments inferred for the Muwaqqar Formation, deposited during the Maastrichtian through the Early Paleocene. The Muwaqqar Formation ranges in thickness from 60 m (Zalmout & Mustafa, 2001) to 780 m (Powell, 1989) and consists of chalk interbedded with chert, marl, and limestone, indicating an open marine condition during the Maastrichtian. The exceptional preservation of fossil taxa suggests low oxygen content at the seafloor (Kaddumi, 2009). The predominance of chalk, combined with the lack of benthic macrofauna, lack of erosional surfaces, and the abundance of plankton indicates a moderately deep pelagic environment (Powell, 1989). This is also supported by macrofossils indicating a paleowater depth of less than 100 m (Kaddumi, 2009).

Diagnosis—*Inabtanin alarabia* is identified as an azhdarchoid pterosaur based on a long, edentulous beak and a humerus with a deltopectoral crest that originates from a distally placed position on the shaft and is rectangular, flat, and elongate in shape. *Inabtanin alarabia* differs from other azhdarchoids based on the presence of a deep laterally compressed lower jaw, short cervical vertebrae (length-to-width ratio that is less than 5), and gracile distal wing bones (length-to-width ratios of at least 10).

Etymology—*Inabtanin* is named for the geomorphological structure near the locality where the specimen was collected, which is called Tal Inab ("grape hill") owing to its prominent coloration. The generic name combines the Arabic words *inab*, for grape, and *tanin* for dragon. Allusions to dragons are common in pterosaur etymology and so *tanin* was chosen to reflect the Arabic language of Jordan, and because of its similarity to the English word *tannin*, derived from the French

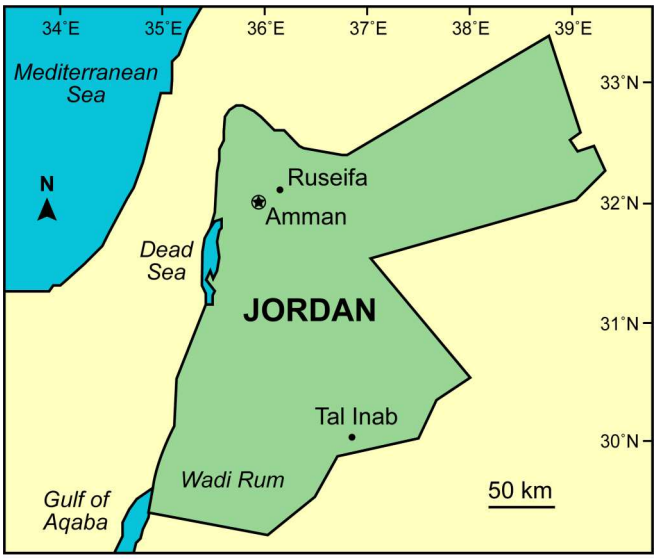

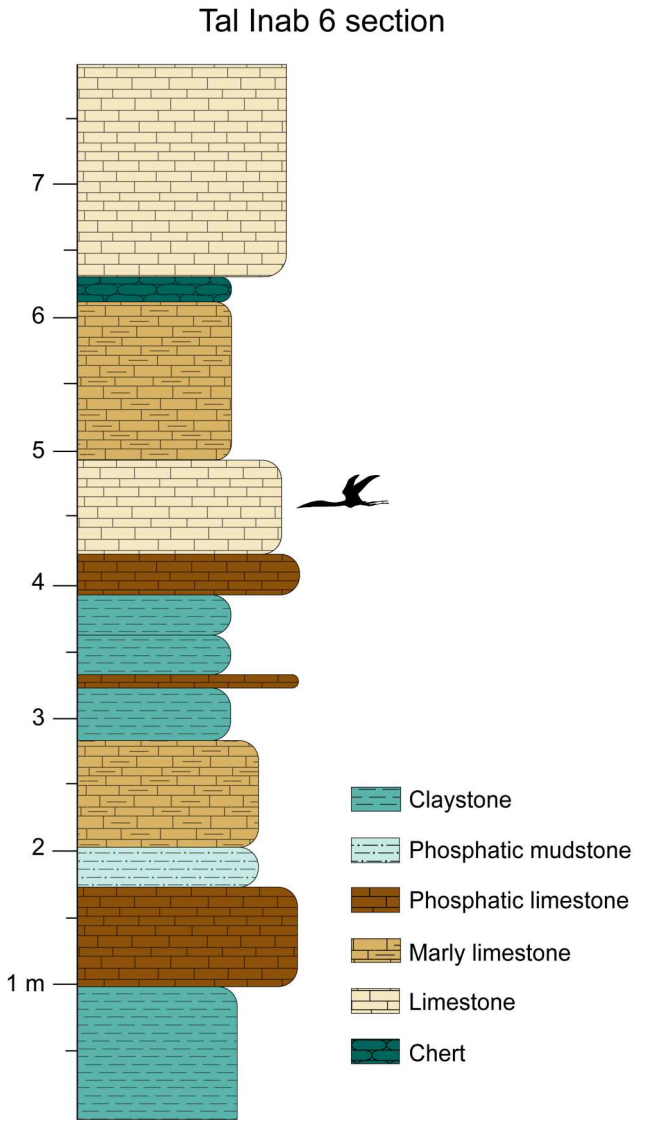

FIGURE 1. Map of Jordan showing pterosaur-bearing fossil localities, the Ruseifa Phosphate Mines and Tal Inab 6, and the stratigraphic section for the Inab site. Pterosaur icon indicates position of *Inabtanin alarabia* holotype in section.

tanin which relates to coloration. The generic name translates to both grape-dragon and grape-colored. The specific name *alarabia* was chosen in reference to the Arabian Peninsula.

DESCRIPTION

Inabtanin alarabia was discovered partially in situ (Fig. 2), with additional material recovered by sieving from the scree slope directly below. The in situ material included the upper and lower jaws, a cervical vertebra, the right radius, the distal portion of the right fourth metacarpal, and the right first wing phalanx. The upper and lower jaws were preserved in occlusion, and the upper jaw was subject to a higher degree of erosion than the lower jaw and limb bones, especially on the dorsal and posterior surfaces. The scree contained two additional cervical vertebrae, the left scapulocoracoid, both humeri, the right ulna, and the proximal right fourth metacarpal. Elements collected from the scree are missing cortical bone, leaving behind a matrix-based natural cast of the bones that contain many surface details and preserve complex articular surfaces. A similar preservation pattern is present in pterosaur bones from Bahariya, Egypt (Salem, 2023:fig. 2.5). Individual pieces collected from the scree could be fit to one another to form nearly complete elements (e.g., the ulna). Measurements are summarized in Table 1.

We hypothesize that *Inabtanin* represents a single adult individual based on size-independent criteria for the maturity of large pterodactyloids (Bennett, 1993). These include the presence of a fully fused scapulocoracoid and epiphyses of the appendicular bones. This is particularly evident in the fusion of the extensor process on the proximal end of the first wing phalanx, which is one of the last fusions to occur before an individual reaches skeletal maturity (Bennett, 1993). Additionally, the articulations are smooth as opposed to pitted, indicating the bones are fully ossified.

This description uses the directional terms outlined in Figure 3. The default posture assumes wings outstretched in flight position, so that surfaces of the wing bones facing the leading edge of the wing are called “anterior,” and those facing the trailing edge of the wing are called “posterior.” We avoid the use of terms such as “cranial,” “caudal,” and “rostral,” in favor of terms that are consistent across all bones and body regions (Wilson, 2006). Features of the skull will be described as “anterior” and “posterior.”

Cranial Bones

The skull is represented by the upper and lower jaws, preserved anterior to the nasoantorbital fenestra (Fig. 4). Based on rostral proportions in other edentulous pterosaurs (e.g., *Quetzalcoatlus*, Andres & Langston, 2021), this represents at least 80% of the skull length. We identify the upper jaw by the presence of the ventral margin of the nasoantorbital fenestra preserved on the left side; the lower jaw is identified by the presence of the symphysis and mandibular rami. The jaws show evidence of pneumaticity, revealed in CT images (see below) as well as fortuitous breaks in the cortical bone (ca. 2 mm thick) that reveal underlying trabecular bone (average >1 mm thick) and irregularly shaped, variably sized alveoli. The alveoli are variable in shape; some are circular (2 mm diameter) or ovular (5–10 × 2 mm), and others are highly irregular (maximum 10 mm).

The jaws are elongate, edentulous structures that together form an elongate pyramid in lateral view that is broadest at the preserved proximal end and tapers to a fine point at its terminus. Near the preserved base, the lower jaw is twice as deep as the upper jaw. At the jaw tip, they are subequal in dimensions. The occlusal margin, as seen in lateral view, is sharp and straight.

FIGURE 2. Photograph of in situ skeletal remains of *Inabtanin alarabia* including cranial material (towards bottom of image), one cervical vertebra (bottom center left of image), and a nearly complete wing (towards top of image).

As discussed below, medial to this edge both the upper and lower jaw are recessed.

Upper Jaw—The preserved portion of upper jaw is nearly half a meter long by 50 mm wide and tall. It consists of a premaxilla and maxilla (Fig. 4). The dorsal margin is nearly completely preserved, but its apex is missing, which we estimate to be an additional few millimeters. What remains of the dorsal margin is a 12 mm wide ridge that tapers to 6 mm at the anterior break. The upper jaw maintains a subtriangular cross section throughout its length. The upper jaw tapers to a point that is broken off, leaving a triangular cross section (12 mm × 10 mm). We estimate that only 4 mm is missing distally.

In cross-sectional view, the occlusal surface is highly concave at the anterior end, with sharp occlusal margins defined by ventrally directed ridges that are 1 mm wide. This curvature flattens entirely at the posterior end. There are no nutrient foramina on the occlusal surface. The posterolateral surfaces of the upper jaw have no mediolateral curvature, and no nutrient foramina are identifiable, but this may be because the cortical bone has been eroded. At the preserved posterior margin of the upper jaw, a small (45 mm) portion of the left nasoantorbital fenestra is represented by a thin margin of bone (23 × 9 mm) with a laterally compressed, triangular cross-section.

Lower Jaw—The preserved portion of the lower jaw consists of the dentary, including the symphysis and rami, but not the articulations with postdentary bones. The lower jaw reaches its maximum preserved depth posterior to the symphysis, where it is nearly twice as deep as it is wide (99 mm × 58 mm). The anterior end of the dentary tapers transversely and dorsoventrally to its preserved end, which is triangular in cross section and 1.8 mm tall by 12 mm wide. The lower jaw retains this cross-sectional shape throughout its preserved length.

Right and left occlusal margins are parallel to one another in dorsal view towards the anterior end of the lower jaw. Posteriorly, they bend away from one another to become concave laterally near their midlength. The occlusal margins are sharp and oriented vertically near the anterior end of the lower jaw, flaring slightly laterally towards the posterior end. The occlusal margins are offset vertically from the flattened, more medial portion of the lower jaw, creating a shallow trough in cross-sectional view. This trough is deepest near the preserved midpoint of the lower jaw, shallowing anteriorly and posteriorly from that point. There is a subtle median ridge within this trough that extends along the posterior half of the symphyseal portion of the lower jaw. There are no pits or foramina visible on the occlusal surface.

The lower jaw tapers ventrally to a median ridge 1–2 mm wide and is 99 mm deep at the posterior end, just anterior to the symphysis. The lateral surfaces of the dentary are finely textured, due to underlying trabecular structure revealed by the eroded cortical bone. Several small (2 mm) nutrient foramina punctuating the lateral surfaces of the lower jaw are concentrated near the posterior occlusal margin. These do not exhibit any pairing or alternating arrangement.

The posterior margin of the dentary symphysis is U-shaped in dorsal view, with a maximum transverse width of 61 mm. The rami are preserved for 91 mm on the left side and 138 mm on the right side. The rami are thin, laterally compressed and flare slightly laterally. They measure 8 mm wide by ca. 36 mm high, and so the rami have a maximum height that is about one-third of the maximum height of the dentary.

Axial Bones

Three cervical vertebrae were collected, one of which has a fragment of the subsequent centrum preserved in articulation (Fig. 5). This latter, well-preserved vertebra resembles middle cervical vertebrae of an unnamed tapejarid, especially positions 5 and 6 (AMNH 22568; Vila Nova et al., 2015:fig. 2). It was found in situ with the cranial material and wing bones (Fig. 2); the other two cervical vertebrae were collected from the scree immediately adjacent to the in situ material. These isolated, partially preserved elements are more challenging to place within the cervical series. One of them appears to be similar in position to cervical vertebra 5/6 and could reasonably be placed

TABLE 1. Measurements (mm) of *Inabtanin alarabia* (YUPC-INAB-6-001–010).

Element	Measurement	mm
Upper Jaw	Preserved length	495
	Length anterior to nasoantorbital fenestra	425
	Width, maximum preserved	50
	Depth, maximum preserved	49
Lower Jaw	Preserved length	499
	Length anterior to the symphysis	361
	Maximum preserved width	58
	Maximum preserved depth	99
Atlantoaxis	Length, anteroposterior, preserved	48
	Width, anterior	30
	Width, posterior	26
	Width, minimum	24
	Height, dorsoventral, preserved	40
	Diameter of neural canal	7
Cervical vertebra 3	Length, preserved	50
	Height, preserved	34
Cervical vertebra 4	Length, preserved	67
	Width of centrum, minimum	24
	Width, posterior	48
	Height, preserved	36
	Diameter of neural canal	7
Scapulocoracoid (L)	Length, dorsoventral	82
	Width, anteroposterior	42
Humerus (L)	Length, minimum	237
	Length, estimated	241
	Diameter, anteroposterior (minimum)	27
	Diameter, dorsoventral (minimum)	30
	Deltopectoral crest, width, mediolateral	40
Humerus (R)	Shaft diameter, anteroposterior (minimum)	27
	Shaft diameter, dorsoventral (minimum)	31
Radius (R)	Length	361
	Proximal diameter, dorsoventral	39
	Proximal diameter, anteroposterior	19
	Shaft diameter, dorsoventral (minimum)	17
	Shaft diameter, anteroposterior (minimum)	10
	Distal diameter, dorsoventral	35
	Distal diameter, anteroposterior	22
Ulna (R)	Length, estimated	369
	Proximal diameter, dorsoventral	66
	Proximal diameter, anteroposterior	33
	Shaft diameter, dorsoventral (minimum)	22
	Shaft diameter anteroposterior (minimum)	17
	Distal diameter, dorsoventral	54
	Distal diameter, anteroposterior	23
Metacarpal IV (R)	Length, estimated	545
	Proximal diameter, dorsoventral	47
	Proximal diameter, anteroposterior	38
	Shaft diameter, dorsoventral (minimum)	18
	Shaft diameter anteroposterior (minimum)	12
	Distal diameter, dorsoventral	28
	Distal diameter, anteroposterior	46
Wing phalanx I (R)	Length, estimated	681
	Proximal diameter, dorsoventral	84
	Proximal diameter, anteroposterior	67
	Shaft diameter, dorsoventral (minimum)	10
	Shaft diameter anteroposterior (minimum)	18
	Distal diameter, dorsoventral	18
	Distal diameter, anteroposterior	28

immediately in front or behind it. Its size and the shape of its condyle suggest that it could be anterior to cervical vertebra 5/6 in the series, perhaps in the fourth or fifth position. The other

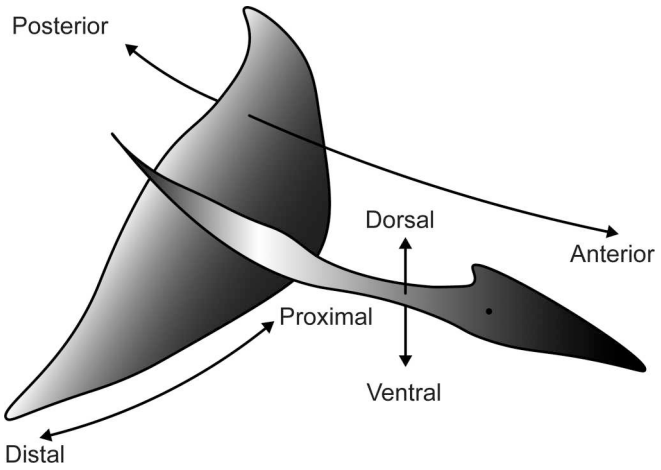

FIGURE 3. Generalized pterosaur body plan in flight position with arms and legs extended, labeled with the directional terms used in this description. Here we use "anterior" and "posterior" in place of "cranial" and "caudal" so that directional terms are consistent throughout cranial and postcranial bones.

isolated axial element is shorter than cervical vertebra 5/6 but bears a larger neural canal, which in reptiles expands near the limb girdles (Giffin, 1990). It is likely that this vertebra is a posterior cervical vertebra, perhaps the seventh, based on comparisons with articulated partial cervical series AMNH 22568 (Vila Nova et al., 2015).

Cervical Vertebra 4 or 5—A small (46 mm long) fragment preserving part of the neural arch and centrum represents the posterior right quarter of cervical vertebra 4 or 5. The centrum preserves a lateral pneumatic foramen, the base of an exapophysis, and half of the posterior condyle. The neural arch preserves a portion of the neural spine and the base of the postzygapophysis. This vertebra is estimated to be slightly smaller than cervical vertebra 5/6 (see below).

The preserved centrum is 7 mm long by 2 mm wide, and if it were complete, it would form a compressed oval in cross section. The lateral surface of the centrum is concave both anteroposteriorly and dorsoventrally. It contains one lateral pneumatic foramen, located at its midlength. The ventral surface of the centrum contains the posterior concavity, which is defined by the bases of the exapophyses. Half of the posterior articulation is preserved as a dorsoventrally compressed condyle (preserved 13 mm width × 8 mm height). The right lateral end of the condyle is confluent with a saddle-shaped articular surface on the dorsal side of the exapophysis (10 mm long × 4 mm wide).

A fragment of the neural arch remains on the right side, where it is low and compressed onto the centrum. As in cervical vertebra 5/6 (see below), the neural arch does not extend as far posteriorly as the centrum. The neural spine is represented by a low ridge that is narrowly pinched (2 mm wide) at the posterior end. The thin lamina leading to the base of the postzygapophysis is preserved on the right side. It is emarginated posteriorly and forms the dorsolateral border of a 15 mm deep pneumatic cavity. A bit of very thin cortical bone is preserved in this pneumatic space. The dorsal surface of the neural arch is concave between the spine and the postzygapophysis and between the postzygapophysis and the presumptive prezygapophysis. The lateral extent of the neural arch is defined by the "postzygoprezygapophyseal" lamina, which connects prezygapophyses and postzygapophyses (Tschopp, 2016). The breadth of the vertebra across this lamina exceeds that of the centrum.

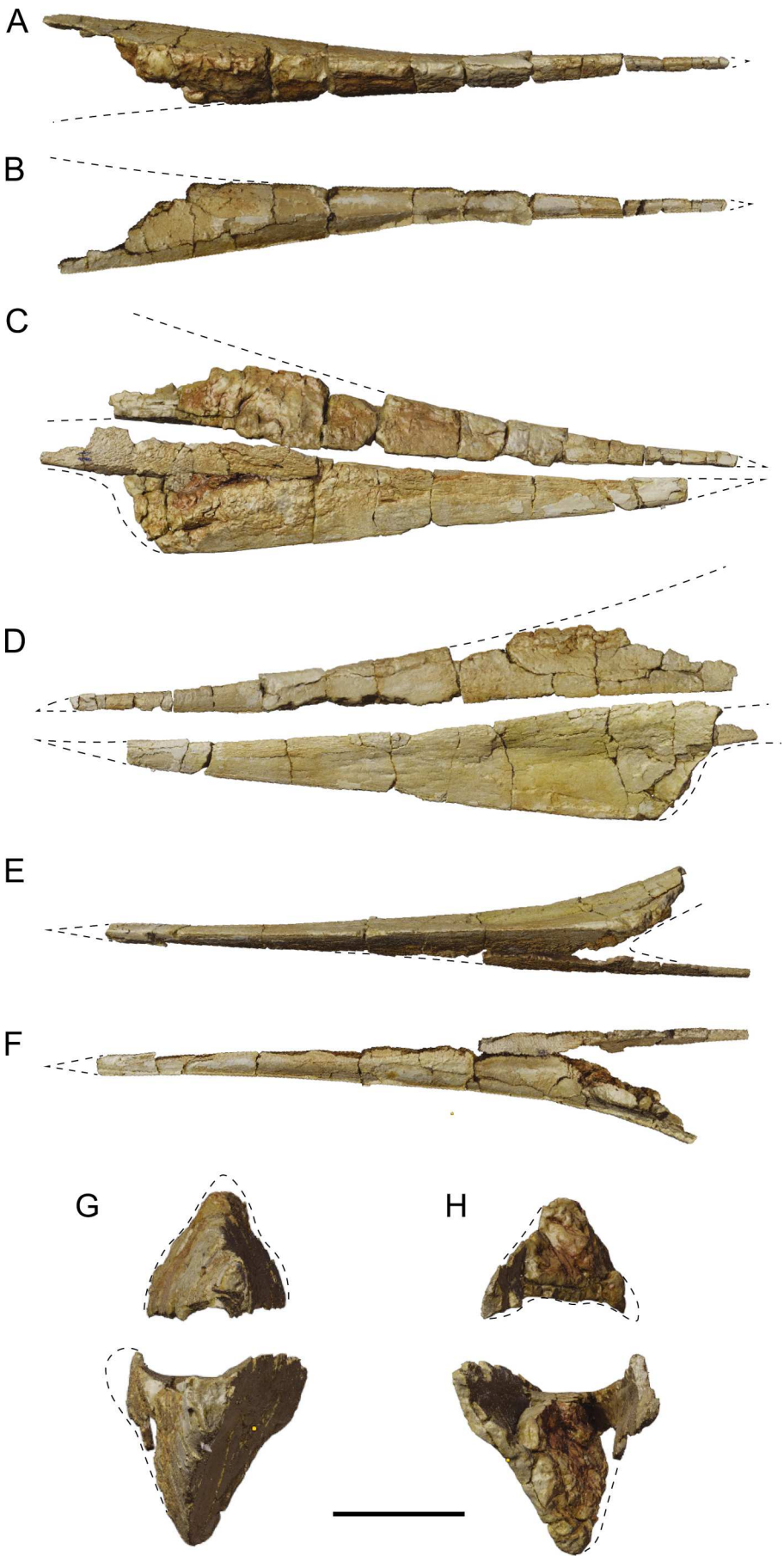

FIGURE 4. *Inabtanin alarabia* cranial material (YUPC-INAB6-001, -002). Photogrammetric reconstruction of the upper jaw in **A**, dorsal view; and **B**, ventral view. Photogrammetric reconstruction of the paired upper and lower jaws in **C**, right lateral view; and **D**, left lateral view. Photogrammetric reconstruction of the lower jaw in **E**, ventral view; and **F**, dorsal view. Photogrammetric reconstruction of the paired upper and lower jaws in **G**, anterior view; and **H**, posterior view. Dashed lines indicate reconstructed outline of bone. Scale bar equals 5 cm for **A**–**F**; 3 cm for **G**–**H**.

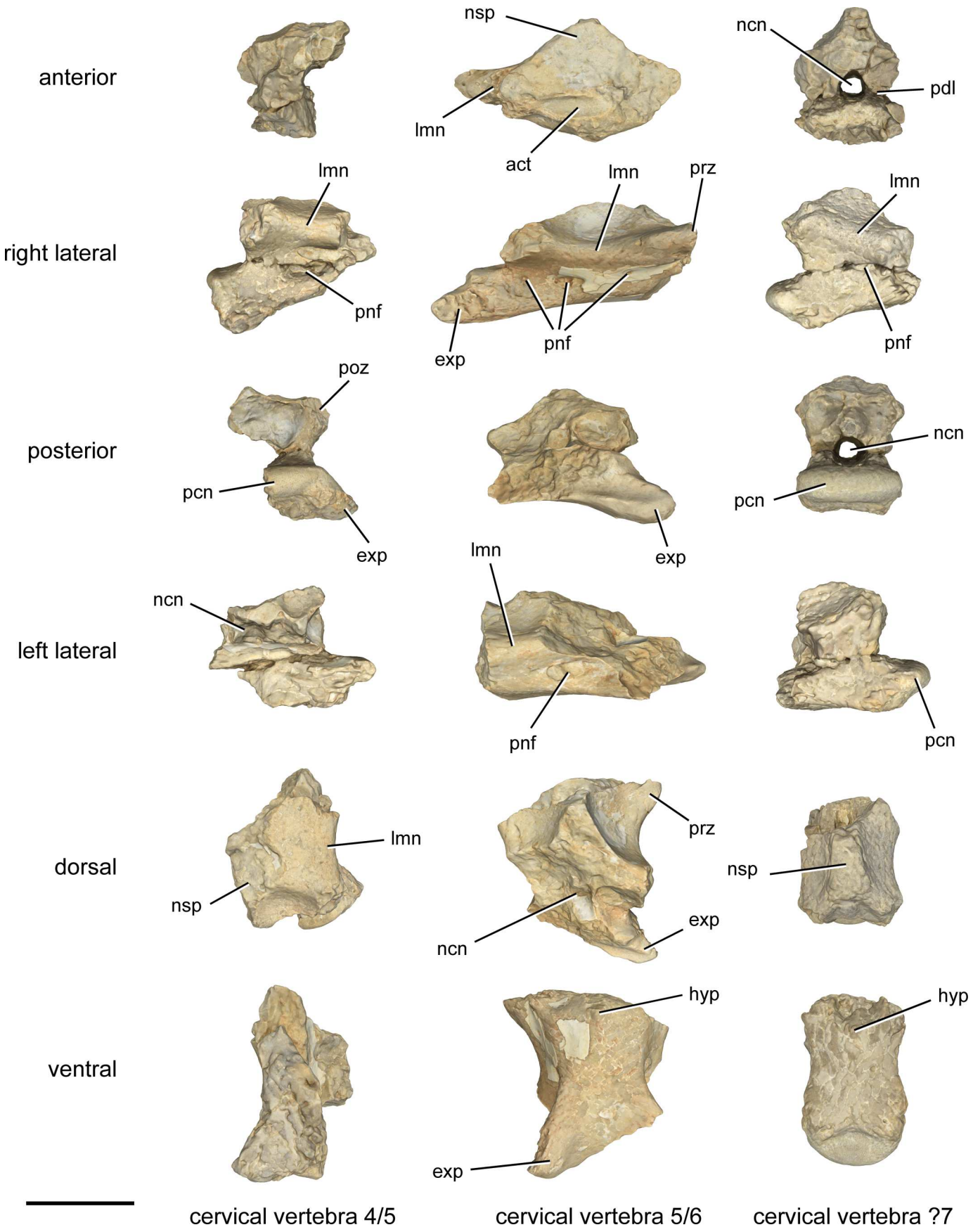

FIGURE 5. *Inabtanin alarabia* cervical vertebrae (YUPC-INAB6-003, -004, -005). Photogrammetric reconstruction of cervical vertebra 4 or 5 in the left column, cervical vertebra 5 or 6 in the center column, and cervical vertebra ?7 in the right column. Note that the images for cervical vertebra 5/6 were created prior to fitting on the attached fragment of the subsequent vertebra mentioned in text. **Abbreviations**: **act**, anterior cotyle; **exp**, exapophysis; **hyp**, hypopophysis; **lmn**, lamina; **ncn**, neural canal; **nsp**, neural spine; **pcn**, posterior condyle; **pdl**, pedicle; **pnf**, pneumatic foramen; **poz**, postzygapophysis; **prz**, prezygapophysis. Scale bar equals 2.5 cm.

The right half of the neural canal is preserved and suggests a circular cross section, whose diameter changes little along the length of the vertebra. Owing to preservation, it is not known whether there are paired pneumatic foramen flanking the neural canal.

Cervical Vertebra 5 or 6—The most complete and best preserved cervical vertebra was collected in situ near the posterior end of the articulated jaws. This vertebra includes a partial neural arch and a nearly complete centrum, lacking only a section of the condyle and the lateral extremes of its anterior end. The neural arch has been broken obliquely and lacks its posterior left side. It preserves the base of the neural spine and most of the right prezygapophysis. The neural canal and pneumatic structures on the centrum and neural arch are well preserved. A small fragment of the subsequent centrum is preserved in articulation, offering the only glimpse at the intercentral contact between cervical vertebrae. As discussed above, this vertebra seems to be positioned in the middle part of the cervical series, perhaps as the fifth or sixth.

The centrum is 60 mm long measured from cotyle to condyle; it is slightly longer including the exapophyses (67 mm). The centrum is roughly hourglass shaped in ventral view, reaching a minimum transverse width of 23 mm and a maximum width of 48 mm. The elongation index (length/transverse width) is 2.6. The centrum is procoelous, with a concave anterior articulation (i.e., the cotyle), and a convex posterior articulation (i.e., the condyle). The cotyle is a shallow, dished structure that is more than twice as broad transversely as it is tall dorsoventrally (ca. 22 × 7 mm). Although its margin is broken, it appears to be tapered ventrally, such that its dorsalmost width is greater than its ventralmost. Just below the lateral edge of the cotyle is a fairly conspicuous pneumatic foramen approximately 2 mm in diameter. On the midline, just ventral to the cotyle, is a subtriangular broken region that represents a midline keel or hypopophysis. It continues as a low but definitive ridge until about mid-centrum. The cortical bone in this region is missing, revealing a crosshatched network of fine (1 mm) trabecular bone. The crosshatches are oriented approximately 45° with respect to the vertebral axis.

The lateral surface of the centrum is pierced by three foramina, as best viewed on the right side. The largest of these is a fairly large, ovoid structure (6 mm long × 4 mm tall) opening at roughly midlength on the centrum. The depth and surrounding fossa suggest it is a pneumatic opening. Slightly posterior to it, near the base of the neural arch pedicle, is a much smaller opening that may also be pneumatic in nature. The third opening is located anterior to the large, central opening. It is also oval in outline and measures approximately 2 × 1 mm. The anterior margin of this foramen extends anteriorly as a shallow but conspicuous groove that wraps around the dorsolateral corner of the anterior centrum, into the large, triangular pneumatic space between the prezygapophyses and neural spine (see below).

The posterior portion of the centrum is partly obscured by the articulated anterior centrum of the succeeding vertebra, but key details of the condyle and exapophyses are visible. The dorsal portion of the posterior centrum is developed into a prominent condyle that extends posteriorly and slightly dorsally. It is elliptical, measuring 7 mm tall by approximately 30 mm wide (estimated by doubling the width of the completely preserved left half). The lateral extremes of the condyle are separated from the convex postexapophyses by a shallow embayment visible in dorsal view. In articulation, this embayment is filled by a similarly shaped convexity lateral to the cotyle on the subsequent centrum. None of the three more complete vertebrae completely preserve these para-cotylar convexities, but a small portion is preserved on the right side of the anterior end of this vertebra, as best seen in ventral view. A relatively small prominence on the right ventrolateral edge of the centrum is situated between a small foramen on the ventral centrum and the groove wrapping anteriorly from the lateral centrum. That groove separates the para-cotylar prominence from the base of the prezygapophysis. Based on comparisons with other pterosaurs, the groove likely represents the transverse foramen, and the prominence is the fused cervical rib (e.g., *Quetzalcoatlus*, Andres & Langston, 2021; *Hatzegopteryx*, Naish & Witton 2017).

The ventral surface of the centrum is concave between the exapophyses, gradually flattening by the midpoint of the centrum. The exapophyses are ca. 7 mm in diameter and project laterally and slightly ventrally, extending posteriorly beyond the condyle. They articulate lateral to the cervical ribs of the subsequent centrum.

The preserved neural arch includes the base of the neural spine, most of the right prezygapophysis, a portion of the right postzygapophysis, and the "postzygoprezygapophyseal" lamina connecting them. A portion of the "postzygoprezygapophyseal" lamina is preserved on the left side as well, implying a minimum transverse width of 37 mm for the neural arch. Even at its narrowest point, the neural arch is wider than the centrum, and it is shifted forward relative to it such that the prezygapophyses extend beyond the cotyle and the postzygapophyses would terminate slightly anterior to the condyle. The base of the neural spine is at least 17 mm long anteroposteriorly. It broadens anteriorly (10 mm) and posteriorly (11 mm) from its narrowest point (8 mm). The lateral portion of the neural arch, between the "postzygoprezygapophyseal" lamina and the neural spine, is gently concave in both the anteroposterior and dorsoventral sense. No pneumatic foramina were visible within this fossa, and so it is not certain whether an air sac was housed there.

The anterior face of the neural arch is predominated by a triangular pneumatic fossa that is bounded by the two prezygapophyses and the neural spine. This fossa is approximately twice as wide as it is tall (35 × 17 mm) and contains within it several pneumatic openings as well as the neural canal. The pneumatic openings are arranged in an arch around the dorsal margin of the neural canal, extending from there in a line towards the prezygapophysis. Most of these are fairly large but irregularly shaped openings (ca. 4 mm long axis) that approach the size of the neural canal, which is nearly 6 mm in diameter.

The right prezygapophysis lacks only its articular surface. It is a small, round nub (8 mm diameter) that extends anteriorly beyond the cotyle and laterally much further than the centrum. The prezygapophyseal articular surface would have been oriented slightly ventrally. The prezygapophysis and postzygapophysis are connected by the postzygoprezygapophyseal lamina, which is rounded and nearly 1 cm thick. The base of the right postzygapophysis originates from this lamina and a much thinner lamina (2 mm) that connects to the centrum. The postzygapophysis is oriented laterally and extends beyond the centrum. Just internal to the postzygapophysis, lateral to the posterior opening of the neural canal, opens a large, elliptical pneumatic foramen (8 × 5 mm).

Posterior Cervical Vertebra (7th?)—This vertebra was found in the scree below the in situ material, and cortical bone is worn away from all surfaces save a small portion within the neural canal. This vertebra includes most of the centrum and much of the neural arch, but lacks its various projections (i.e., zygapophyses, exapophyses, neural spine). The neural canal and posterior centrum articulation are completely preserved.

The posterior cervical vertebra is pentagonal in anterior and posterior views and hourglass shaped in dorsal and ventral views. The centrum is damaged at its anterior end, and so the shape of the articular surface is unknown. The preserved

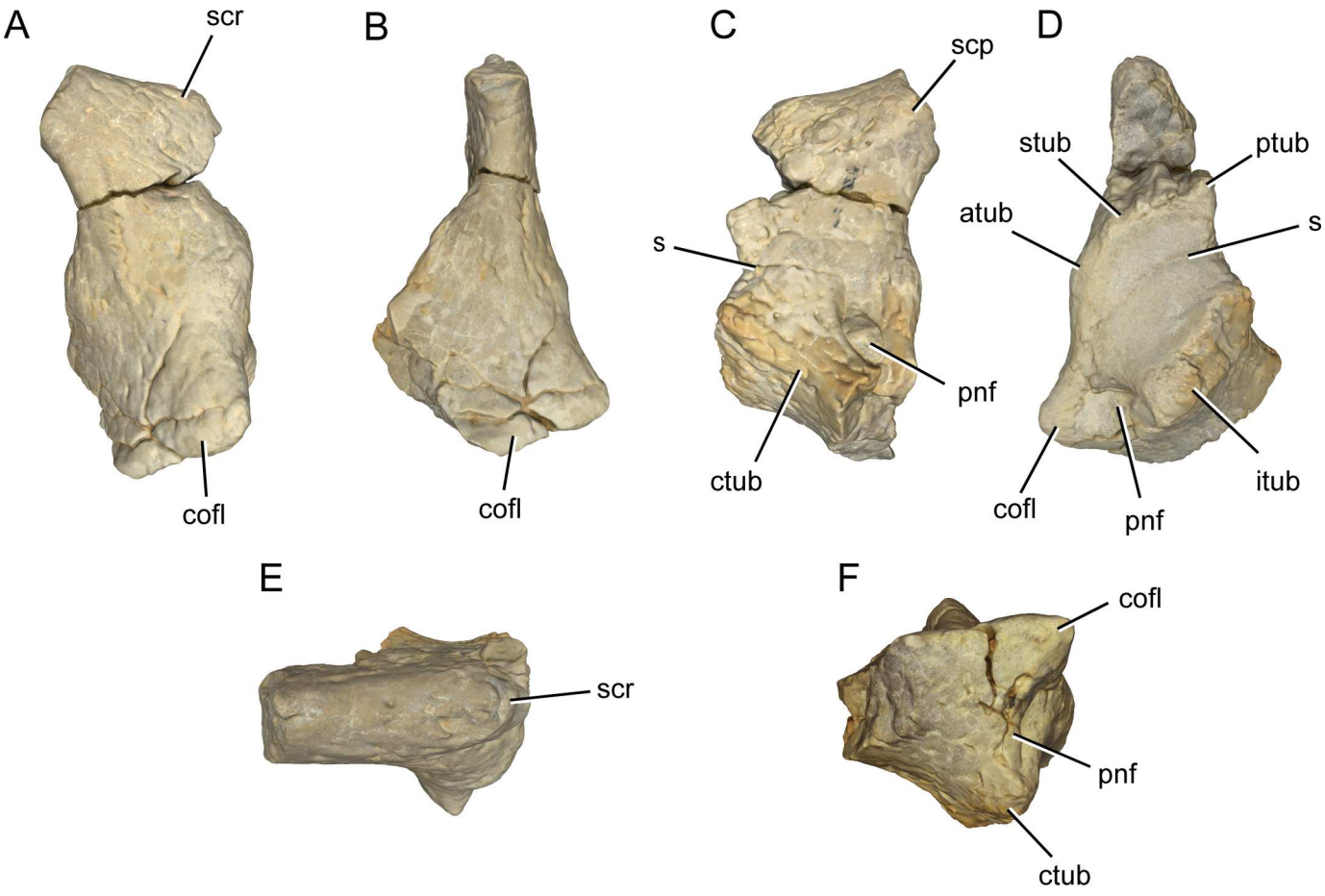

FIGURE 6. *Inabtanin alarabia* left scapulocoracoid (YUPC-INAB6-006). Photogrammetric reconstruction in **A**, anterior view; **B**, medial view; **C**, posterior view; **D**, lateral view; **E**, dorsal view; and **F**, ventral view. **Abbreviations**: **atub**, anterior lesser tubercle; **cofl**, coracoid flange; **ctub**, coracoid tubercle; **itub**, infraglenoid tubercle; **pnf**, pneumatic foramen; **ptub**, posterior lesser tubercle; **s**, suture; **scp**, scapular process; **scr**, scapular ridge; **stub**, supraglenoid tubercle. Scale bar equals 2 cm.

portion of the centrum is subrectangular in cross section, measuring roughly 30 mm wide by 13 mm tall. The centrum is pinched at the midpoint (22 mm) relative to the ends (ca. 29 mm), which results in a nearly symmetrical hourglass shape. There are two openings near the neurocentral junction that may represent lateral pneumatic foramina, as best seen on the right side (Fig. 5). The ventral surface of the centrum is smooth and slightly transversely convex. Towards the anterior third of the ventral centrum is a low ridge leading to a broken area that may represent the hypopophysis. The bases of paired exapophyses are situated ventral to the posterior condyle and extend ventrally and posteriorly. The posterior condyle is a well-preserved articular surface on a dorsoventrally compressed tab (25 × 9 mm) extending posteriorly with a dorsal inclination.

The neural spine is damaged, but we estimate that when complete, it would have been more than 7 mm tall, less than 8 mm wide, and 20 mm long. The lateral aspect of the neural arch is concave both dorsoventrally and anteroposteriorly, as can be seen in dorsal or anterior views. The concave lateral margin of the neural arch is formed by the "postzygoprezygapophyseal" lamina. The neural arch is transversely widest at the anterior end (estimated to be at least 34 mm) and narrowest at the midpoint (28 mm). The pedicles are each 6 mm thick and together correspond to the medially pinched minimum transverse width of 20 mm. The posterior end of the neural arch is dorsally elevated, where the pedicles are 12 mm high. The postzygapophyses are not preserved, but their bases provide a maximum posterior width of at least 31 mm.

The neural canal is circular. It measures 7 mm in diameter at the anterior opening and expands slightly to 9 mm at the posterior opening. A small (4 mm) pneumatic foramen opens dorsal to the posterior opening of neural canal.

Appendicular Bones

Scapulocoracoid—A partial left scapulocoracoid was collected from the scree below the in situ material (Fig. 6). It is missing the cortical bone and the distal ends of the scapular and coracoid processes. The scapulocoracoid is identified by the distinct laterally facing glenoid, which bears a transversely oriented suture between the scapula and coracoid, and large pneumatic foramina. The glenoid is angled by roughly 45° relative to the vertical axis of the bone. The scapula is oriented dorsally, the coracoid is oriented ventrally, and both are inclined medially.

The scapular blade is thin and supported by an anteroposteriorly compressed, elliptical base (25 × 16 mm). The scapula is

smooth and flat on its anterior surface. There is a 12 mm-wide scapular ridge that leads to the anterior supraglenoid tubercle on its dorsolateral face. The scapular process on the posterior face is wide and low, and it was continuous with the posterior supraglenoid tubercle of the glenoid fossa.

The glenoid is concave, with a trapezoidal articular surface defined by the anterior and posterior lesser tubercles and the supraglenoid and infraglenoid tubercles (Fig. 6D). The glenoid is 43 mm tall by 27 mm wide and deeply concave at the posterior half. The scapulocoracoid suture is fused but patent and cuts across the middle of the glenoid, following a shallow sinusoidal path. The suture is not visible on the anterior surface, but it is faintly visible on the posterior surface. In the absence of cortical bone, we can see fine (1 mm) trabecular bone that is densely packed near the articular surface and sparse elsewhere. A large, elliptical, transversely oriented pneumatic foramen (24 × 10 mm) opens just anteroventral to the glenoid. The opening is deep and is subdivided into smaller cells by struts. There are numerous 1–2 mm nutrient foramina covering the non-articular surface.

The coracoid is supported by a wide, compressed, irregularly shaped base. The orientation of the base of the coracoid suggests that the bone would have extended medially and twisted posteriorly in relation to the scapula. The distal coracoid is missing, and the break reveals a D-shaped cross section (40 × 19 mm). The base of the coracoid is predominated by a prominent, laterally pointing coracoid flange ventral to the glenoid. On the posterior surface of the coracoid there is a large, ovoid pneumatic foramen (21 × 9 mm).

Humerus—Partial right and left humeri are preserved. They both are weathered and lack cortical bone; the surface of the preserved internal humerus is smoothed. The left humerus is the more complete element, preserving nearly its entire length in two pieces separated by a small gap. A third piece that appears to pertain to the distalmost deltopectoral crest is also preserved, again with a gap separating it from the remainder of the element. The right humerus is represented by its proximal third, including the neck of the proximal articular head, the proximal articular tuberosity, proximal shaft, and the base of the deltopectoral crest. Together these two elements provide information to provide a fairly complete description of the humerus and to reconstruct its anatomy in three dimensions (Fig. 7). The description below is based on the more complete left humerus, unless otherwise noted.

The two shaft pieces of the left humerus do not have a snap-fit with one another, but their cross-sectional shape, coloration, and texture indicate they pertain to the same element. Similarity in the diameters of their opposing faces and comparisons with humeri of other azhdarchoids (e.g., *Quetzalcoatlus*; Andres & Langston, 2021:fig. 30) suggest that little is missing. The length of the humerus is estimated to be 241 mm, with a maximum proximal width of 74 mm, a minimum diameter of 27 mm, and a distal width at least 52 mm.

In proximal view, the humerus is L-shaped, with the ventrally projecting proximal tuberosity and the anteriorly projecting deltopectoral crest forming the arms of the "L" and the articular head at the apex joining them (Fig. 7E). The proximal articular head is wide and round, with a smooth convex surface. The posterior margin of the articular head is expanded and overhangs the shaft, whereas the anterior margin is nearly confluent with the shaft. The proximal tuberosity is quite narrow (17 mm) near its base at ventral margin of the proximal articular head. From there, it pinches slightly to its minimum width (11 mm) before expanding to its maximum width of 23 mm. The anterior and posterior surfaces of the proximal tuberosity in this region are concave, smooth, and pneumatic, although no foramina are preserved here. Where the proximal tuberosity meets the humeral shaft, it produces an ulnar crest that descends along the shaft.

The deltopectoral crest extends anteriorly from the shaft. Its long axis is oriented perpendicular to the long axis of the shaft. Relative to other pterosaurs, the base of the deltopectoral crest is transversely narrow (37 mm) and distally displaced; it is separated from the proximal articular head by at least 25 mm. The deltopectoral crest is slightly better preserved on the right humerus, where its exposed cross section is elliptical (37 × 16 mm). The piece attributed to the distalmost left deltopectoral crest has a squared distal margin that is teardrop shaped in anterior view (Fig. 7A). We estimate the deltopectoral crest is two times longer than its transverse width based on the dimensions of the preserved sections on both humeri.

The shaft of the left humerus has a variable cross-sectional shape. The shaft near the deltopectoral crest base is slightly D-shaped in cross section where the anterior shaft surface is slightly flattened and the dorsal, posterior, and ventral surfaces are rounded into an arc. The shaft tapers to its minimum dimensions (27 × 30 mm) proximal to the midpoint, where the cross section is subcircular. The shaft is interrupted by a sharp break near the midpoint, where it is 30 mm in diameter—the same dimensions as the corresponding break on the distal half. The subcircular cross section continues along the shaft until the entepicondyle and ectepicondyle expand dorsally and ventrally from the shaft, returning it to a D-shape cross section at the distal end. The distal end is so highly eroded that it is entirely formed of the matrix infilled natural cast and is not reflective of the true anatomy. There it reaches maximum dimensions of 52 mm in dorsoventral height and 36 mm in anteroposterior width. It does not preserve the morphology of the epicondyles, capitulum, or trochlea.

The left humerus preserves the internal anatomy well, so we can observe pneumatic structure on the exposed surface. There, a network of trabecular bone is visible. Some trabecular bone is exposed as small hollow circles (2 mm diameter), and other areas terminate trabeculae at an oblique angle revealing 2 mm wide tubes extending across the shaft.

Radius—The right radius is complete except for most of the cortical bone, patches of which remain on the shaft surface (Fig. 8). Most of the preserved bone is the matrix-filled natural cast of the interior volume. The length of the radius is 361 mm, 20 times as long as the minimum diameter of the shaft. The shaft remains narrow and straight throughout its length. The articulations expand dorsoventrally from the shaft, and the proximal end is slightly dorsally inflected relative to the long axis of the bone.

The proximal radius is characterized by a prominent dorsal expansion, the radial tubercle, that tapers to a blunted end (Fig. 8D). The proximal one-sixth of the radial shaft is dorsally inflected, accentuated by tuberosities along its ventral margin (Fig. 8B, D). The more prominent of these, the ventral tuberosity, peaks at 35 mm from the proximal end of the radius. The anterior and posterior tuberosities lie side by side and are smaller and situated more proximally on the radius (Fig. 8C). The trough formed between them continues distally towards the ventral tuberosity. In articulation with the ulna, these three tuberosities line up with prominences on the ulna (see below, "Ulna"). The radial tubercle is a dorsally pointing projection that ends in a small plateau. The articular surface of the radial tubercle is exposed dorsally and posteriorly. It is convex and oriented obliquely relative to the long axis of the shaft. The proximal articular surface of the radius is teardrop shaped, tapering dorsally towards the radial tubercle. The ventral or cotylar portion of the articular surface is markedly concave ventral region, gradually flattening dorsally and becoming convex towards the radial tubercle. The anterior margin of the cotyle is high and rounded compared with the posterior margin, which has a lower and sharper edge. In

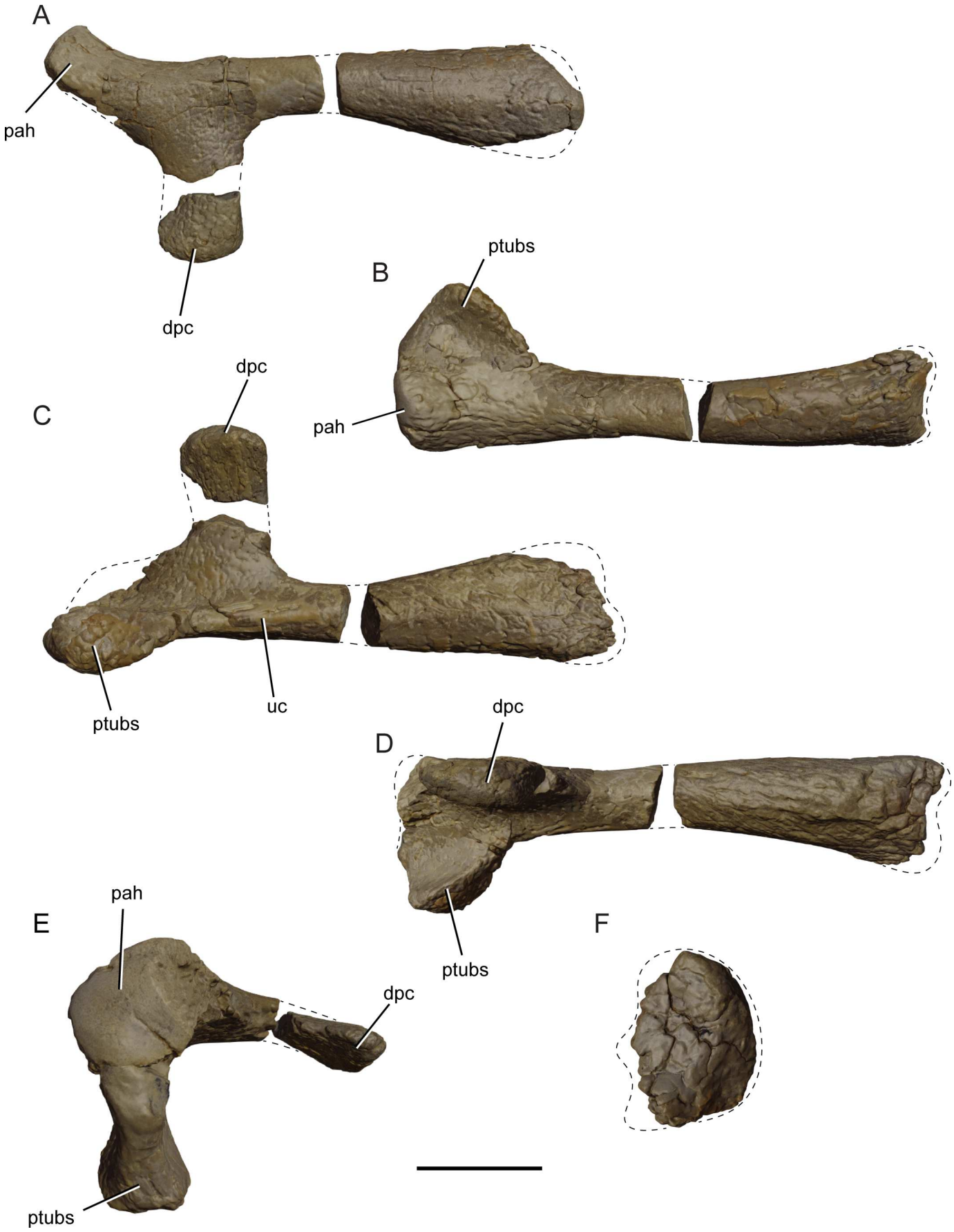

FIGURE 7. *Inabtanin alarabia* humerus (YUPC-INAB6-007, -008). Blender model combining photogrammetric reconstructions of the right and left humeri in **A**, dorsal view; **B**, anterior view; **C**, ventral view; **D**, posterior view; **E**, proximal view; and **F**, distal view. Dashed lines indicate reconstructed outline of bone. **Abbreviations**: **dpc**, deltopectoral crest; **pah**, proximal articular head; **ptubs**, proximal tuberosity; **uc**, ulnar crest. Scale bar equals 5 cm for **A**–**D**; 3 cm for **E**–**F**.

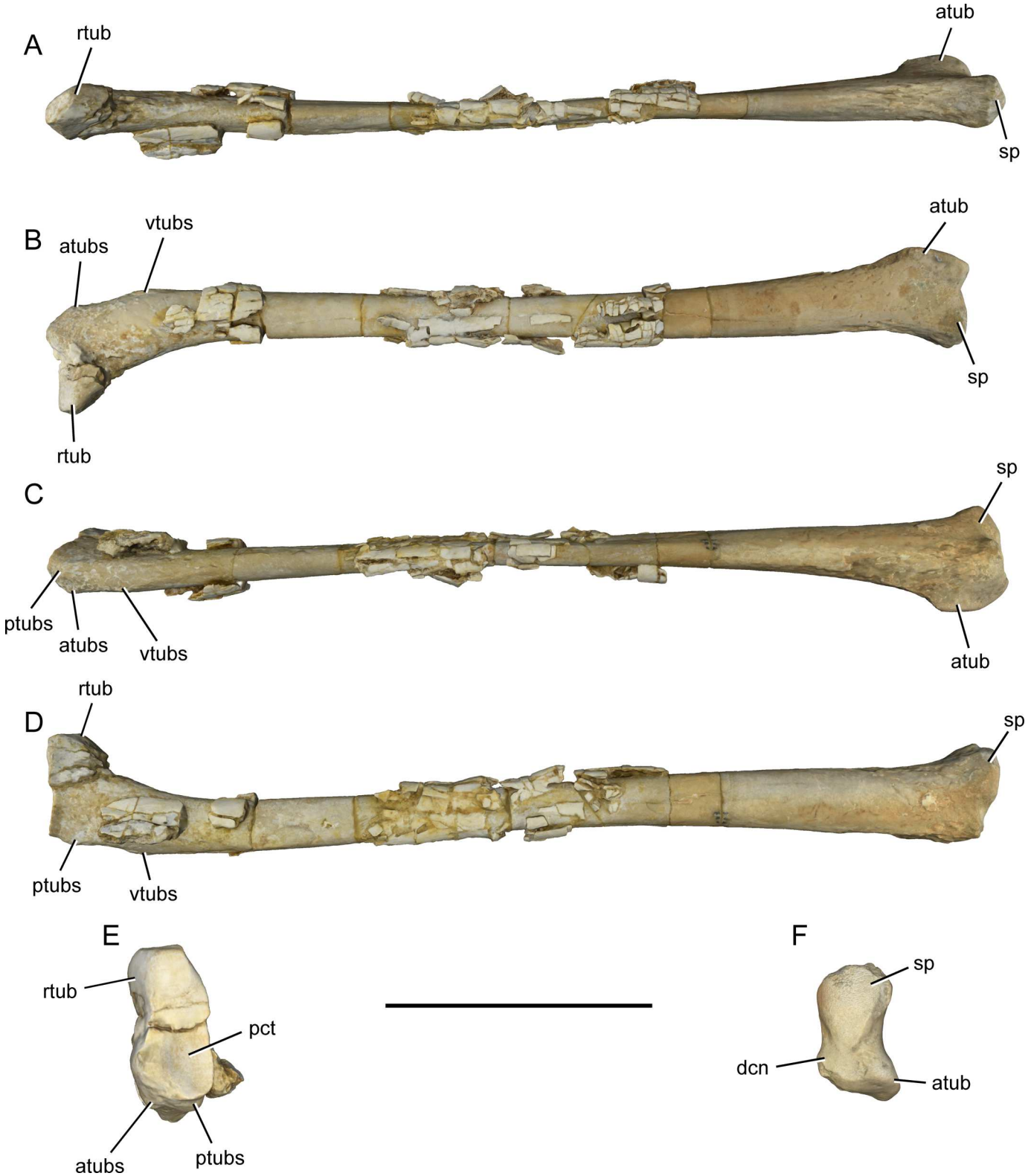

FIGURE 8. *Inabtanin alarabia* right radius (YUPC-INAB6-009). Photogrammetric reconstruction in **A**, dorsal view; **B**, anterior view; **C**, ventral view; **D**, posterior view; **E**, proximal view; and **F**, distal view. **Abbreviations**: **atub**, anterior tubercle; **atubs**, anterior tuberosity; **dcn**, distal condyle; **pct**, proximal cotyle; **ptubs**, posteroventral tuberosity; **rtub**, radial tubercle; **sp**, styloid process; **vtubs**, ventral tuberosity. Scale bar equals 10 cm for **A**–**D**; 7.5 cm for **E**–**F**.

articulation, the radial cotyle would be contiguous with the dorsal portion of the ulnar cotyle (see below, "Ulna").

The radial shaft has an elliptical cross section that is flattened anteroposteriorly. It bows slightly dorsally (Fig. 8D) and has no anteroposterior curvature (Fig. 8A, C). The shaft margins are parallel from near the proximal end to the midshaft before expanding through the distal two-fifths to produce the distal articulation.

The distal end of the radius is expanded dorsoventrally (42 mm) and to a lesser extent anteroposteriorly (23 mm) relative to the shaft. The distal expansion is asymmetrical in both anterior and posterior views (Fig. 8B, D). The dorsal portion of the distal radius expands gradually, reaching its greatest breadth near the end of the element and forming a rounded styloid process that is convex anteriorly, posteriorly, dorsally, and distally (referred to as the "tubercle" by Andres & Langston, 2021). The ventral expansion of the distal radius, in contrast, begins more proximally on the shaft and increases more abruptly than does the dorsal expansion. From its point of maximum expansion, it tapers towards the distal terminus of the element. A delicate, slightly sigmoidal crest extends from the ventral aspect to the anterior and distal portions of the distal radius, forming a reversed 'J' shape in ventral view. This structure has been termed the "anterior tubercle" in *Azhdarcho* (Averianov, 2010) or the "anterior tuberosity" in *Quetzalcoatlus* (Andres & Langston, 2021).

The distal articular surface of the radius forms an asymmetrical hourglass shape in distal view. The dorsal portion of the hourglass, formed by the styloid process, is teardrop shaped and convex. The articular surface extends onto the anterior and posterior surfaces of the distal radius (Fig. 8B, D). The ventral portion of the distal articular surface, formed by the anterior tubercle, is smaller and less rounded than is the dorsal portion. Like the dorsal portion of the distal articular surface, it extends onto the posterior surface of the radius, where it is expanded into the hemispherical distal condyle (Fig. 8D).

Although no foramina are preserved, the structure of the cortical and trabecular bone indicates the element was pneumatized. The cortical bone preserved along the shaft is 2 mm thick, white in color, and chalky in texture. Below the cortical bone, the trabecular bone is visible. The trabeculae are denser at the articulations and enclose alveoli that are elongate or tubular in shape and 1–3 mm in length. Where they are visible in the shaft, the trabeculae are 1 mm thick and do not enclose alveoli but rather extend as struts throughout. The struts are hollow, as visible where some struts terminate in circular or oblique cross section (0.5 mm diameter) at the exposed shaft.

Ulna—The right ulna is nearly complete, consisting of two pieces separated by a small gap located towards the proximal end of the shaft (Fig. 9). There is damage to the posterior face of the proximal end, and as a result the olecranon process is not completely preserved. On the posterior side of the distal end, some of the bone forming the perimeter of the pneumatic foramen is damaged. As a result, the size and shape of that opening are distorted. The ulna would have been approximately 369 mm long, based on interpolation of the gap separating the two preserved shaft pieces and using the articulation with the radius as a constraint on length. The ulna is a gracile element with a shaft diameter that is less than one-tenth its length. Both the proximal and distal ends expand dorsoventrally from the shaft, the proximal end more so than the distal.

The proximal ulna is roughly D-shaped in cross section, with a flattened anterior face and rounded posterior face. The anterior face of the ulna bears a clearly marked area for contact with the radius, buttressed on its ventral side by the block-like ventral process. Two prominences, or tuberosities, rise on the dorsal margin of ventral process of the proximal ulna (Fig. 9B, C). In articulation, the more proximal of these two tuberosities lines up with the anterior and posterior tuberosities of the radius, and the more distal of the two lines up with the ventral tuberosity of the radius (see above, "Radius"). A small pneumatic opening appears to be present just dorsal of the ventral process of the proximal ulna, near the flattened area for articulation of the radius. The proximal ulna is expanded dorsally to accommodate the dorsal tubercle of the radius.

The humeral articular surface of the proximal ulna is subtriangular to crescentic in outline, containing two articular areas separated by an intercotylar crest (Fig. 9E). The more dorsal of these, the dorsal cotyle, is triangular and defined by the dorsal tuberosity, the intercotylar crest, and the olecranon. It is tipped anteriorly, which may have limited the degree of extension at the elbow. The anterior margin of the dorsal cotyle (33 mm) is low, smooth, and curved in a very slight distal arc until the ventral margin at the intercotylar crest. Its posterior margin (30 mm) terminates in a low, rounded bulb adjacent to the olecranon process. Its ventral margin is poorly defined, but appears to be interrupted by a ridge that protrudes dorsally, forming the margin of a small depression (11 × 7 mm). Owing to the absence of cortical bone, the definitive margin of the articular surface is difficult to trace here. The intercotylar crest is 17 mm long and oriented anterodorsally to proximoventrally. The surface texture of the crest indicates a high degree of abrasion, but it appears to have connected with the olecranon process. The ventral cotyle (27 × 16 mm) is rhomboidal in shape and defined by the intercotylar crest and the ventral process. The cotylar surface is concave and tipped anteroventrally. The concavity is deepest dorsally and becomes shallower ventrally. Again, owing to the lack of cortical bone the precise margins of the articular surface are difficult to define. The olecranon process is damaged, as indicated by a sharp break in its posterior margin. The arched surface of the posterior portion of the ulnar shaft is low and smooth, indicating that the olecranon did not project far proximally or posteriorly.

The shaft of the ulna is oval in cross section throughout its length and elongated dorsoventrally. It bows anteriorly, reaching the peak of its arc proximal to midlength, where the shaft narrows to its minimum diameter (22 × 17 mm). From this point, the shaft diameter increases gradually in the dorsoventral plane, where the cross section is increasingly elliptical at the distal end.

The distal ulna is expanded into asymmetrical dorsal and ventral condyles (Fig. 9B, D). The dorsal condyle expands gradually to its inflection point, before tapering sharply towards the distal articular surface. The ventral condyle, in contrast, begins expanding slightly more proximally than does the dorsal condyle and reaches a blunted inflection point more proximally. It tapers very gradually at first, and then more abruptly closer to the distal end of the ulna. The distal condyles of the ulna are separated by a U-shaped notch. A large pneumatic foramen opens between the distal condyles on the posterior surface of the ulna (Fig. 9D). Dorsal and ventral tuberosities project from their respective condyles. The dorsal tuberosity is broad and shallow (16 cm wide) and terminates in a flat, rounded peak. The ventral tuberosity forms a flange that is inflected anteriorly, with a concave anterior surface and a convex posterior surface. The ventral tuberosity extends for 50 mm and reaches a maximum width of 14 mm proximal to the ventral condyle. A tuberculum is present on the anterior face of the dorsal condyle. There is a narrow depression between the tuberculum and the dorsal tuberosity, and the shaft is gently concave across the comparably broader stretch between the tuberculum and ventral tuberosity.

The articular surface of the distal ulna is peanut-shaped (Fig. 9F). The dorsal condyle is sigmoidal (19 × 33 mm), and its

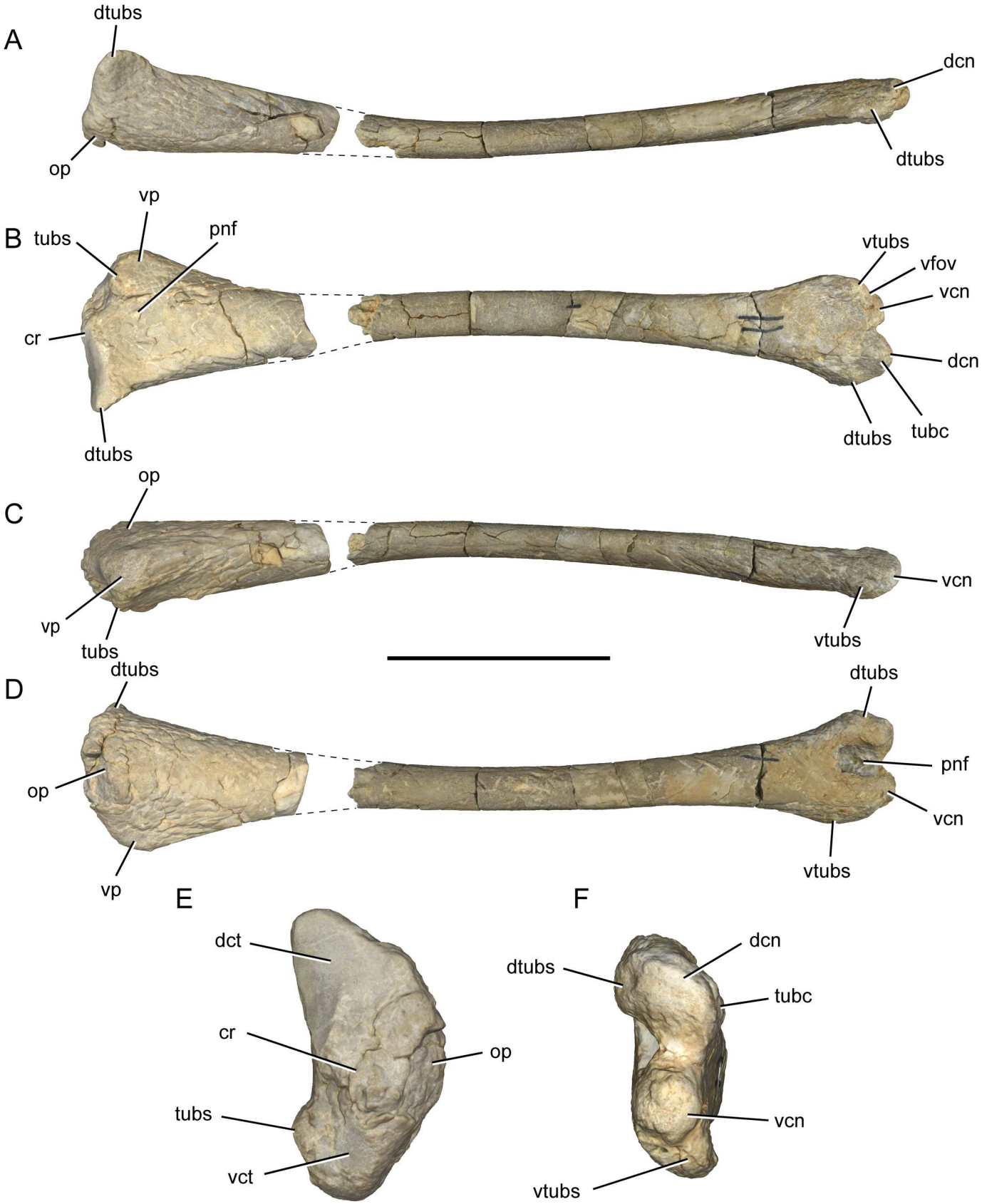

FIGURE 9. *Inabtanin alarabia* right ulna (YUPC-INAB6-010). Photogrammetric reconstruction in **A**, dorsal view; **B**, anterior view; **C**, ventral view; **D**, posterior view; **E**, proximal view; and **F**, distal view. Dashed lines indicate reconstructed outline of bone. **Abbreviations**: **cr**, intercotylar crest; **dcn**, dorsal condyle; **dct**, dorsal cotyle; **dtubs**, dorsal tuberosity; **op**, olecranon process; **pnf**, pneumatic foramen; **tubc**, tuberculum; **tubs**, tuberosity; **vcn**, ventral condyle; **vct**, ventral cotyle; **vfov**, ventral fovea; **vp**, ventral process; **vtubs**, ventral tuberosity. Scale bar equals 10 cm for **A**–**D**; 5 cm for **E**–**F**.

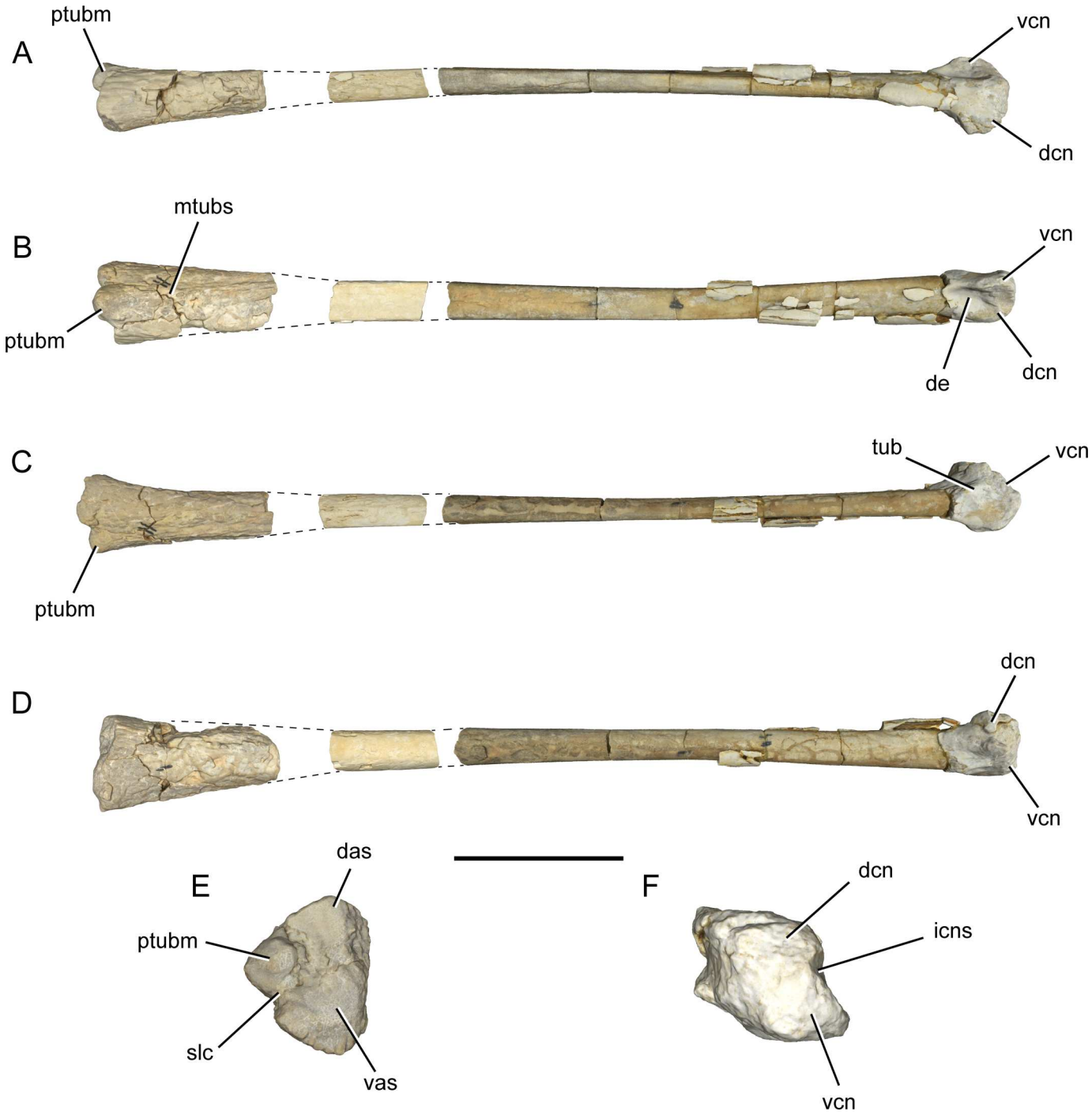

FIGURE 10. *Inabtanin alarabia* right fourth metacarpal (YUPC-INAB6-011). Photogrammetric reconstruction in **A**, dorsal view; **B**, anterior view; **C**, ventral view; **D**, posterior view; **E**, proximal view; and **F**, distal view. Dashed lines indicate reconstructed outline of bone. **Abbreviations**: **das**, dorsal articular surface; **dcn**, dorsal condyle; **de**, depression; **icns**, intercondylar sulcus; **mtubs**, median tuberosity; **ptubm**, proximal tuberculum; **slc**, sulcus; **tub**, tubercle; **vas**, ventral articular surface; **vcn**, ventral condyle. Scale bar equals 10 cm for **A**–**D**; 5 cm for **E**–**F**.

articular surface is oriented so far posteriorly that it is not visible in anterior view. This indicates that the wrist joint would have had very limited mobility in the anterior direction. The ventral condyle is a small round bulb (15 mm diameter) that points distally and is distinct from the ventral tuberosity by a small indentation that contains a 2 mm ventral fovea. The trough between the two condyles is smooth and 10 mm deep anteroposteriorly.

The ulna is highly pneumatic. The cortical bone is entirely abraded away, exposing the trabecular bone underneath. The visible trabecular bone indicates a much greater density of bone tissue at the articulations than within the shaft. There are some visible struts (1 mm) in the midshaft. The trabeculae enclose elongated alveoli in the proximal and distal ends of the ulna. The alveoli decrease in length towards the articulations, becoming rounder at the articular surfaces.

Metacarpal IV—The right metacarpal IV consists of three pieces separated by two gaps in the proximal shaft (Fig. 10). The largest piece, pertaining to much of the shaft and the distal

end, was collected in situ with other wing elements and the jaws. Cortical bone is preserved on the distal end and in small amounts along the shaft. The other two pieces, pertaining to the proximal end and a portion of shaft, were collected from scree on the slope below the in situ material. There is almost no cortical bone on these two pieces, but details of the proximal articular surface are interpretable from the preserved surface.

Metacarpal IV is at least 545 mm long, accounting for the gaps of missing material that are interpolated based on a continuous angle of taper of the shaft dimensions flanking the gaps. The bone is extremely elongate, with a length that is almost 50 times its minimum shaft diameter.

The proximal end of metacarpal IV is triangular in outline, with apices positioned near the dorsal, ventral, and anterior extremes of the element that correspond to the dorsal articular surface, ventral articular surface, and proximal tuberculum, respectively (Fig. 10E). The dorsal articular surface is a ventrally pointing triangle (19 × 14 mm); it is concave and tipped slightly anteriorly. The ventral articular surface is also a ventrally pointing triangle, but its articular surface is convex (rather than concave) and relatively large (26 × 23 mm). The proximal tuberculum is a small and round structure (15 mm diameter) that is set apart from the dorsal and ventral articular surfaces by a crescentic sulcus (Fig. 10E). The proximal tuberculum, along with the dorsal and ventral articular surfaces, fit in corresponding facets on the proximal syncarpal, which was not preserved in this specimen. The proximal tuberculum connects to a median tuberosity on the anterior surface, which extends distally and twists to the ventral margin of the shaft leaving the rest of the anterior shaft flat. The anterior surface of the proximal end is flat or concave to accommodate the smaller metacarpals, which were not preserved.

The shaft is 'D' shaped in cross section along much of its length, with a flattened anterior face. There is very little curvature along its length (Fig. 10A–D), in contrast to the more pronounced sigmoid curvature present in the wing metacarpal of *Quetzalcoatlus* (Andres & Langston, 2021:fig. 38). The shaft narrows gradually to its minimum diameter (13 × 19 mm), which is positioned distal to the midlength, before it expands dorsoventrally towards the distal end. Distal to the point of its minimum diameter, the shaft cross section becomes more elliptical. The ventral surface of the distal shaft bears a V-shaped tubercle that may be associated with soft tissue of the joint between metacarpal IV and the first wing phalanx.

The distal articular surface of metacarpal IV is poorly preserved, despite preservation of cortical bone throughout. The distalmost portions of the two articular condyles have been worn away such that there is little of the intercondylar groove that normally would separate them. They do not articulate well with the first wing phalanx, which is well preserved (see below, "First Wing Phalanx"). The distal articular surface is rotated approximately 30° with respect to the dorsoventral axis of the shaft. It includes asymmetrical dorsal and ventral condyles, both of which expand anteroposteriorly but to different extents. The ventral condyle is slightly larger anteroposteriorly and shifted anteriorly relative to the dorsal condyle (Fig. 10F). In ventral view, the ventral condyle emerges abruptly from the shaft, and its articular surface begins after just before the expansion flattens out. The articular surface wraps around to the posterior surface, but it does not quite reach as far proximally on the shaft as it does anteriorly (Fig. 10D). In dorsal view, the dorsal condyle expands anteriorly much less than does the ventral condyle, and it wraps around to the posterior surface farther than it does on the anterior surface. The intercondylar sulcus is best preserved posteriorly, where it is broad and concave to accommodate the extensor process of the first wing phalanx. A marked depression is present on the anterior surface of distal metacarpal IV, shifted towards the ventral side of the element. This depression would have accommodated the extensor tendon process of the first wing phalanx and resisted hyper-extension of the metacarpal–phalangeal joint.

First Wing Phalanx—A right first wing phalanx is preserved in two pieces, with a distal break in the shaft representing a small amount of missing bone (Fig. 11). The proximal and distal portions have identical cross-sectional shape and size on either side of the gap, indicating that only a small portion is missing.

The first wing phalanx is highly elongated and dorsoventrally compressed; it is estimated to be greater than 680 mm long. This uncertainty is due to the small break in the distal shaft and the high degree of abrasion on the distal articulation. The proximal articulation is the most robust feature of the bone. It is exceptionally well preserved with no discernible distortion and much of the cortical bone intact. Cortical bone is also preserved along the shaft until the distal break. The distal end contains no cortical bone and is represented by a matrix-filled natural cast.

The proximal articular surface of the wing phalanx bears two offset concavities, the dorsal and ventral cotyles, which are separated by a low intercotylar ridge. The extensor tendon process and flexor tendon process are associated with the ventral and dorsal cotyles, respectively (Fig. 11E). The extensor process is fully fused, indicating that this is a skeletally mature individual. The extensor process is subtriangular, with a strong indentation on the anterior side for the attachment of the extensor tendon. Its apex curves posteriorly and would have served to limit extension and brace the leading edge of the wing. The dorsal tuberculum is just distal to the extensor tendon process on the dorsal surface of the wing phalanx, extending quite far down the shaft as a ridge. On the opposite side of the wing phalanx, the flexor tendon process extends ventrally from the ventral cotyle. It is rounded and dorsoventrally compressed; it is placed further dorsally than the extensor process and further posteriorly than the ventral tuberosity. The dorsal cotyle is a 29 × 14 mm concave crescent that extends from the base of the extensor tendon process to the apex of the flexor tendon process. The articular surface has sharp margins and is oriented nearly perpendicular to the axis of the shaft. By contrast, the ventral tuberosity is wider and longer than its dorsal counterpart (35 × 15 mm) and oriented posteriorly. The posterior extent of the ventral cotyle is limited, supporting the folding of the wing. A low ventral tuberosity contributes to the sharp margin of the ventral cotyle. It grades into the shaft near a large, elliptical, proximodistally elongated pneumatic foramen (16 × 8 mm; Fig. 11C). Trabecular bone is visible within the foramen and between the cotyles.

The shaft has an ovoid cross section that is compressed dorsoventrally. The anterior edge is narrower than the posterior edge and defined by the ridge that extends from the dorsal tuberculum. The shaft arcs anteriorly, suggesting resistance to bending in the anteroposterior plane during flight. The shaft reaches a minimum diameter (11 × 19 mm) distal to the midpoint. On both the dorsal and ventral surfaces, there is a thin longitudinal trough indicating some crushing of the shaft during preservation. Near the distal end, the cross section becomes sub-triangular in shape with a flat ventral surface and a low dorsal ridge. The distal end expands anteroposteriorly, reaching a maximum diameter (28 × 19 mm) before becoming rounded and dorsoventrally compressed more distally. This rounded end indicates that the distal articulation was not much longer than what is preserved, despite the high degree of abrasion.

The wing phalanx preserves more cortical bone than any other element. The cortical bone is less than 1 mm thick at the proximal

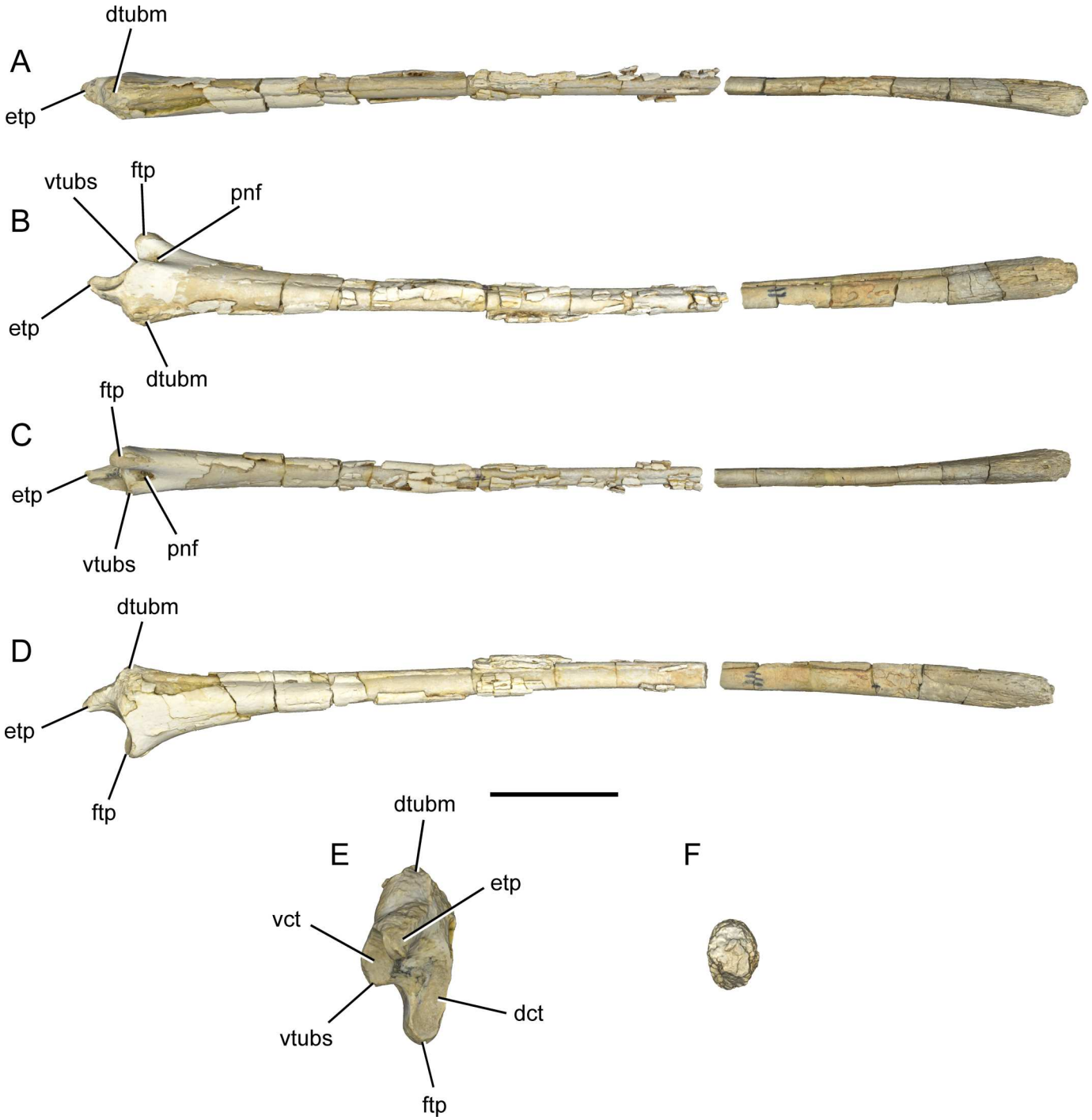

FIGURE 11. *Inabtanin alarabia* right first wing phalanx (YUPC-INAB6-012). Photogrammetric reconstruction in **A**, dorsal view; **B**, anterior view; **C**, ventral view; **D**, posterior view; **E**, proximal view; and **F**, distal view. Dashed lines indicate reconstructed outline of bone. **Abbreviations**: **dct**, dorsal cotyle; **dtubm**, dorsal tuberculum; **etp**, extensor tendon process; **ftp**, flexor tendon process; **pnf**, pneumatic foramen; **vct**, ventral cotyle; **vtubs**, ventral tuberosity. Scale bar equals 10 cm for **A**–**D**; 5 cm for **E**–**F**.

articulation, where it is supported by trabecular bone, and it averages 2 mm thick throughout the shaft. Trabecular bone is visible at the proximal and distal ends of the wing phalanx but appears far less dense than the trabecular tissue of other wing bones, particularly at the distal end. No struts are visible on the surface of the midshaft.

Comparisons

Inabtanin alarabia possesses features typically associated with azhdarchids, such as large body size, an edentulous beak, and the structure of the deltopectoral crest of the humerus. Additionally, the trabecular walls of the wing bones enclose elongated alveoli as reported in other azhdarchids (Buffetaut et al., 2002, 2003).

However, *Inabtanin* lacks other features typically associated with azhdarchids. It retains lateral pneumatic foramina on the cervical vertebrae, which do not have an elongation ratio greater than 5, and it lacks paired nutrient foramina on the mandible (Martill & Moser, 2017). Due to this mix of azhdarchid and non-azhdarchid traits, it is likely that *Inabtanin* is an azhdarchoid that falls outside of Azhdarchidae.

The cranial material of *Inabtanin* overlaps with pterosaurs such as *Aerotitan*, *Alanqa*, *Bakonydraco*, and *Mistralazhdarcho*, which are represented largely by jaw remains. *Inabtanin* lacks a median eminence on the dorsal surface of the lower jaw, which differs from the contemporaneous pterosaurs *Alanqa* and *Mistralazhdarcho*. The distinctive eminence of the anterior jaw of the azhdarchoid *Bakonydraco* also differs significantly from *Inabtanin*. The lack of elongate middle cervical vertebrae also argues against close affinities with long-necked azhdarchoids such as *Albadraco*, *Azhdarcho*, *Cryodrakon*, *Eurazhdarcho*, *Mistralazhdarcho*, *Phosphatodraco*, *Quetzalcoatlus lawsoni*, and *Zhejiangopterus.*

The cervical vertebrae of *Inabtanin* bear the closest resemblance to those of *Hatzegopteryx*. *Inabtanin* is an adult, so it is unlikely that it represents a juvenile of the giant pterosaurs *Arambourgiania*, *Hatzegopteryx*, or *Quetzalcoatlus northropi*. Although its spatiotemporal context draws the closest comparisons with *Arambourgiania*, its humerus is one-third of the size and has a different cross-sectional shape than the *Arambourgiania* specimen described below. In addition, its cervical vertebrae differ greatly from the holotypic vertebra of *Arambourgiania philadelphiae*, which has an elongation ratio of 11 (compared with 2.8 in the *Inabtanin* holotype).

The wing bones of *Inabtanin* appear very gracile in comparison to the more robust wing bones of *Quetzalcoatlus lawsoni*, which shares a similar estimated wingspan. The proximal cotyle of the radius is teardrop shaped as in *Azhdarcho lancicollis* (Averianov 2010), but the dorsally projecting tubercle is relatively less extended.

AZHDARCHIDAE Nesov, 1984
ARAMBOURGIANIA PHILADELPHIAE (Arambourg, 1959) Nesov, Kanznyshkina, & Cherepanov, 1987
(Fig. 12)

Holotype—A middle cervical vertebra (UJA VF1) recovered from the Ruseifa Phosphate Mines (Arambourg, 1959).

Referred Material—Referred remains include YUPC-RUSEIFA-1, a partial right humerus shaft. Previously referred material includes two phalanges, a cervical vertebra (Frey & Martill, 1996); SNSB-BSPG 1966 XXV 501, 503, 506, 507, 508, 512, a proximal metacarpal IV, three probable fragments of cervical vertebrae, a partial femur, and a possible distal radius (Martill & Moser, 2017). We suspect that a fragmentary appendicular bone previously described as a possible ornithopod tibia (Martill et al., 1996) might also pertain to *Arambourgiania*, based on similarity in dimensions, surface details, and spatiotemporal context.

Horizon and Locality—The Ruseifa phosphate mine section is located 7 km NE of Amman. It is composed of the Phosphorite Unit and the overlying Muwaqqar Formation (Fig. 1c). Ruseifa contains four levels of phosphorite that fine upwards and are separated by thinner layers of limestone, marl, dolomite, and chert. Each horizon begins with a cemented and silicified base and becomes well-laminated upwards. Units 3 and 4 display lamination, cross bedding, and erosional surfaces (Zalmout & Mustafa, 2001). All four units yield vertebrate fossils (Bardet & Suberbiola, 2002). The remainder of the section consists of the Muwaqqar Formation represented by chalk, marl, limestone, and chert (Zalmout & Mustafa, 2001). The Ruseifa pterosaur was

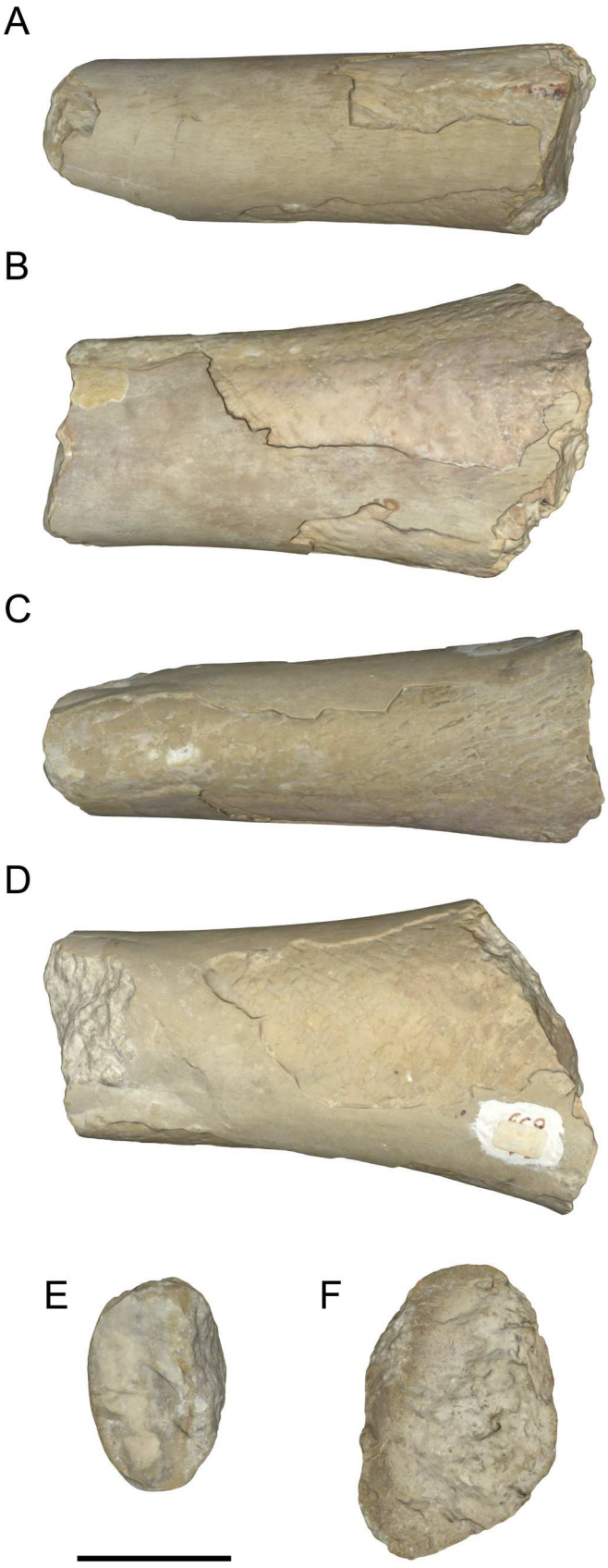

FIGURE 12. *Arambourgiania philadelphiae* right humerus (YUPC-RUSEIFA-001). Photographs in **A**, dorsal view; **B**, anterior view; **C**, ventral view; **D**, posterior view; **E**, proximal view; and **F**, distal view. Scale bar equals 5 cm.

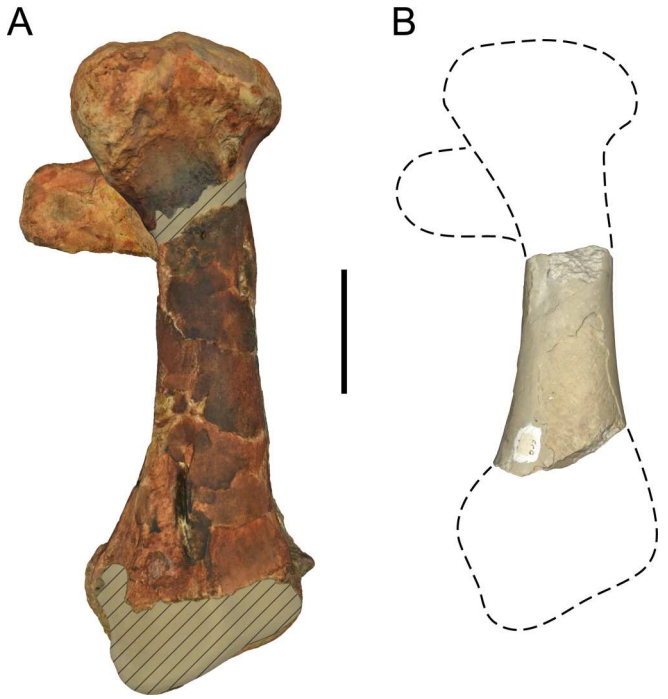

FIGURE 13. Comparison of humeri of giant azhdarchid pterosaurs. **A**, *Quetzalcoatlus northropi* (TMM 41450-3), cast of the left humerus (reversed) in posterior view. **B**, *Arambourgiania philadelphiae* (YUPC-RUSEIFA-001) right humerus in posterior view. Dashed lines indicate reconstructed outline of bone. Diagonal lines indicate broken areas. Scale bar equals 10 cm.

surface collected, and so the stratigraphic origin of this isolated element is not certain. Other giant pterosaur fossils from Ruseifa have been linked to Unit 1 (Frey & Martill, 1996), which has been interpreted as a deep marine environment owing to the lack of near shore sedimentary structures present in Units 3 and 4.

Description—The right humerus shaft is 185 mm long and has the shape of a flattened cylinder that expands distally. The shaft is broken just distal to the deltopectoral crest, where the preserved minimum diameter is found. The cross section of the proximal end is an anteroposteriorly compressed oval (80 × 60 mm). As it expands distally, the cross-sectional shape changes. A posteroventral ridge begins 75 mm from the preserved distal end of the humerus, giving it a subtle D-shaped cross section. As the ridge extends distally, it becomes more prominent and would have been contiguous with the ectepicondyle. The preserved maximum diameter is located at the distal break (119 × 73 mm).

The broken ends of the shaft reveal thin (2 mm) cortical bone. The cortical bone is abraded away on some of the surface of the shaft revealing thin (1 mm) trabecular bone. The trabecular bone forms a crosshatched pattern infilled with matrix. The ratio of matrix to trabecular bone indicates a high proportion of air space, approximately 90% air by volume. Where the structure of the trabeculae is visible, the thin bony walls separate alveoli that range from 1–3 mm in length.

Comparisons—This specimen is identified as pterosaur based on the distinct internal bone structure comprised of thin cortical bone and thinner trabecular bone. This indicates that it possesses an extremely high air space proportion (ASP) that is only found in pterosaurs. Previous studies utilizing μCT scans have exhibited ASPs ranging from 70–90% air in the pneumatized long bones of the largest taxa (Martin & Palmer, 2014a, 2014b). The thin bony walls separate numerous, elongated alveoli similar to the condition described in the giant azhdarchid from Romania, *Hatzegopteryx thambema* (Buffetaut et al., 2002, 2003). The cross-sectional shape and measurements of this specimen compare favorably with the humerus of *Quetzalcoatlus northropi* (89 × 69 mm at minimum shaft diameter) (Fig. 13). We attribute this humerus to *Arambourgiania* because it comes from the holotypic quarry, is of comparable size, and is very similar in shape to that of the closely related species *Q. northropi* (Table 2).

TABLE 2. Measurements of the humeri of *Arambourgiania philadelphiae* (YUPC-RUSEIFA-1) and *Quetzalcoatlus northropi* (TMM 41450-3). An 'i' indicates an incomplete measurement.

Specimen	Measurement	mm
A. philadelphiae	Length	185i
	Minimum diameter, dorsoventral	80
	Minimum diameter, anteroposterior	60
	Maximum diameter, dorsoventral	119
	Maximum diameter, anteroposterior	73
Q. northropi	Length	535
	Minimum diameter, dorsoventral	89
	Minimum diameter, anteroposterior	69

INFERRING FLIGHT CAPACITY AND STYLE

The wings of *Inabtanin* outstretch those of the largest wandering albatrosses by more than a meter (5 vs. 3.5 m). Many of the pterosaurs of the latest Cretaceous represent the upper body size limits of vertebrate flight capacity. This has led to the suggestion that organisms of such extreme body sizes cannot maintain powered flight, based on scaling calculations that the upper limit of body mass for a soaring individual is only 41 kg (Sato et al., 2009). Some body mass estimates indicate that giants like *Quetzalcoatlus northropi* weighed almost 550 kg (Henderson, 2010), although consensus around body mass estimates for giant azhdarchids has settled at an upper limit of 200–250 kg (Martin & Palmer, 2014b; Witton, 2008).

The opposing view that pterosaurs were capable of powered flight at high body masses is supported across many studies, citing retention of flight anatomy in the form of highly pneumatic bones, thin cortical bone, well-developed deltopectoral crests, no reduction of wing bones, as well as modeling flight capacity based on body mass estimates and wing aspect ratio (Alexander, 1998; Buffetaut et al., 2002; Chatterjee & Templin, 2004; Claessens et al., 2009; Geist et al., 2014; Middleton & English, 2015; Naish et al., 2021; Witton, 2008; Witton & Habib, 2010; Witton & Naish, 2008). Additionally, whereas some studies assert the morphology and depositional environments of giant azhdarchids indicate terrestrial locomotion and foraging, they do not claim that these adaptations preclude flight (Naish & Witton, 2017; Witton, 2007; Witton & Naish, 2008). Here we use the internal trabecular bone structure preserved in the two Jordanian pterosaur specimens to evaluate the hypothesis that they were capable of powered flight.

Here, we rely on avian bone structure as an extant analog, because they possess pneumatic bones and share a common archosaurian ancestor, allowing for direct osteological comparison. All categories for flight style in living birds include flapping flight and additionally may include gliding or soaring flight (Pennycuick, 1982). The internal structure of wing bones from modern birds has been explored in model-based materials science research, establishing three categories for the internal trabecular structures that occur in pneumatized wing bones: struts, ridges, or no structures (Novitskaya et al., 2017;

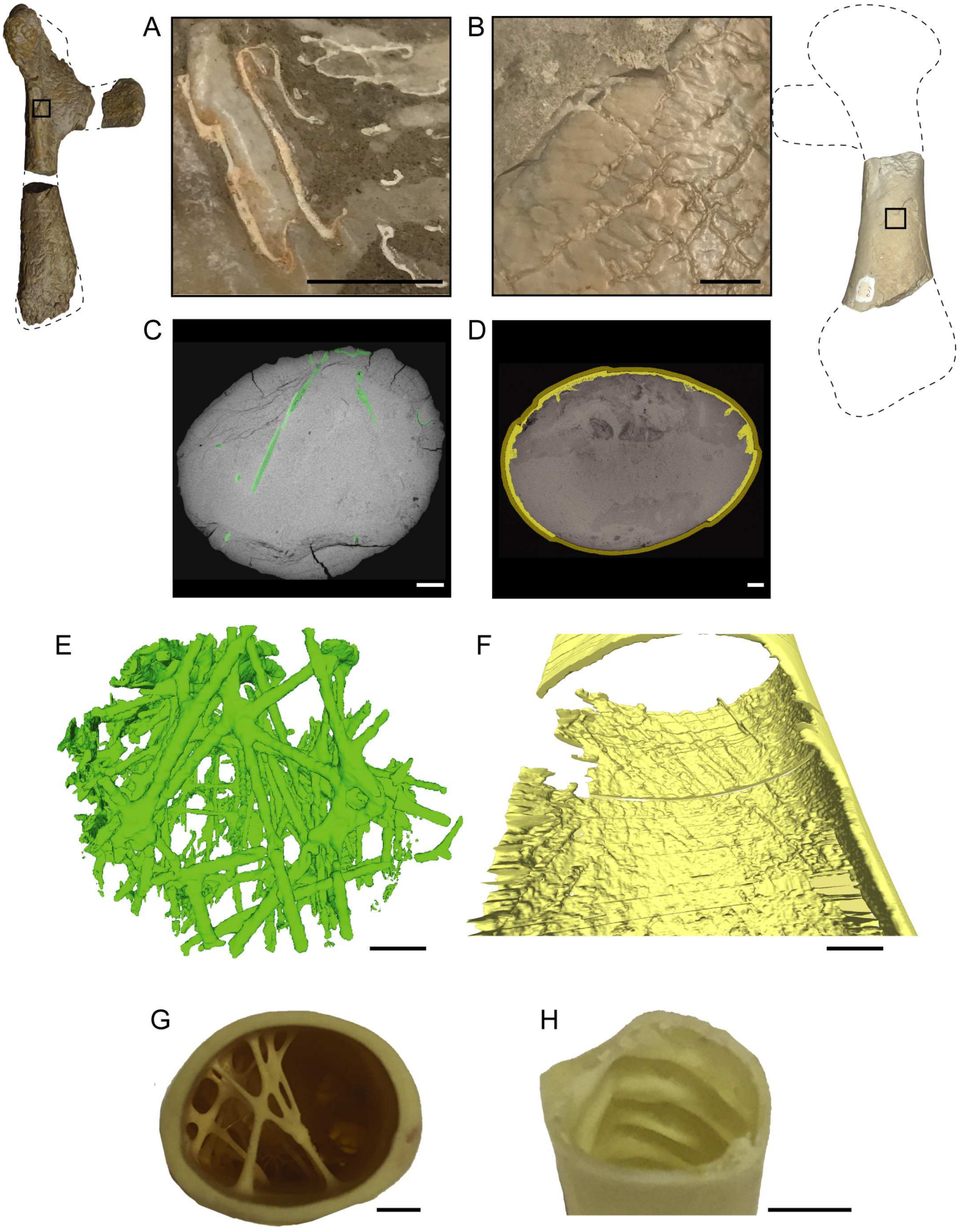
A
B
C
D
E
F
G
H

TABLE 3. Measurements of the angle of intersection of the internal bone structure in the humeri of the Jordan pterosaur species *Inabtanin alarabia* (YUPC-INAB-6-001–010) and *Arambourgiania philadelphiae* (YUPC-RUSEIFA-1).

Specimen	Measurement	Value
I. alarabia	Angle of diaphyseal struts intersection (mean)	83°
	Standard deviation	31
	Angle of epiphyseal struts intersection (mean)	87°
	Standard deviation	24
A. philadelphiae	Angle of ridge intersection (mean)	92°
	Standard deviation	8
	Angle of ridges to long axis (mean)	45°
	Standard deviation	6

Pennycuick, 2008; Proctor & Lynch, 1993; Sullivan et al., 2017). It has been established that bone structure is influenced by mechanical loading (Frost, 1960a, b; Wolff, 1986), so it follows that the formation of internal support structures is the result of adaptive reformation of bone in response to the stress and strain of flight. Volant birds have wing bones that contain networks of perpendicular struts in the shaft supporting the thin cortical bone; non-volant birds lack these structures. The structure and arrangement of these struts have been shown to resist the forces of bending more than those of torsion (Novitskaya et al., 2017). Most volant birds are capable of flapping flight, and so this structural pattern is found across a wide range of body sizes and wing morphologies. Birds that also exhibit a soaring flight style additionally can develop helical ridges in the diaphyses of their wing bones (Sullivan et al., 2017). Birds with lift soaring flight style are generally large and have long wingspans and high wing aspect ratios. Examples include pelagic sea birds and vultures, which rely on thermal currents to support flight by minimizing flapping and the associated mechanical strain. Soaring flight style confers greater relative torsional forces on wing bones than does flapping flight. In stress tests of idealized models, these helical ridges have been shown to withstand torsion (Novitskaya et al., 2017). Additionally, a case study examined the wing bone structure of an individual of a volant species that was not permitted to fly (Kiang, 2013). This individual developed densely packed spongy trabecular bone instead of thin cortical bone with supportive trabeculae. Therefore, we can conclude that the presence of characteristic internal trabecular bone structure is indicative of flight capacity, and that the predominance of either struts or ridges is indicative of the predominant type of mechanical loading a wing bone experiences during flight and may indicate flight style.

Inabtanin—Three-dimensional models of the trabecular bone in the humeri of *Inabtanin* were constructed from μCT scan data, revealing a network of hollow struts with circular cross sections. The struts are thicker and more densely packed at the epiphyses compared with the thinner, more sparsely distributed struts in the diaphysis (see 3D model on University of Michigan Deep Blue Data; https://doi.org/10.7302/c1fs-xb12). The diaphyseal struts range in diameter from 1–3 mm and intersect each other at an average angle of 83°. Epiphyseal struts range in diameter from 2–4 mm and intersect each other at an average angle of 87° (Table 3). For the humerus of *Inabtanin*, the average angle of strut intersection is nearly a right angle. In irregular lattices, it is the average angle of the struts that signifies optimal resistance to bending loads (Bakhvalov et al., 2009).

The arrangement and structure of the struts in the humeri of *Inabtanin* match those found in the wing bones of modern flapping birds (Fig. 14). The presence of these adaptive structures indicates that this individual experienced the bending loads associated with flapping flight, and so it is likely that *Inabtanin* flew by conventional flapping, although this does not preclude occasional use of other flight styles.

Arambourgiania—The humeral shaft of *Arambourgiania* does not possess internal struts, in contrast to that of *Inabtanin*. Instead, a three-dimensional model of the trabecular bone in the humeral shaft of *Arambourgiania* based on μCT data reveals a series of thin ridges lining the cortical bone of the diaphysis. These diaphyseal ridges line the shaft in two opposing helical sets forming a crosshatched pattern that can be seen both on the surface of the bone and within the three-dimensional model (Fig. 14). A sample of these ridges measured in relation to the long axis of the shaft gives an average angle of 45°. One set of helical ridges occurs with greater frequency; these ridges are each 1 mm across and have a left-handed or clockwise chirality. The clockwise ridges are oriented at an average of 43° from the long axis of the humerus. Another, less frequent set of helical ridges are thicker (2 mm) and have a right-handed or counterclockwise chirality. The counterclockwise ridges are angled at an average of 54° relative to the long axis of the humerus. The clockwise and counterclockwise ridges intersect each other at an average angle of 92° (Table 3).

The structure and arrangement of diaphyseal ridges in the humerus of *Arambourgiania* are similar to those found in the wing bones of vultures (Fig. 14), although the height of the ridges is less in the fossil element than it is in the fresh bone specimen. The presence of diaphyseal ridges and absence of struts suggest that, like the vulture, this *Arambourgiania* individual experienced torsional loadings associated with soaring flight. The ridge angle for torsional resistance would be expected to be 45° (intersecting at 90°) if forces loading the wing were equal in both directions. However, we would expect variation in ridge angles if there were asymmetry in the torsional forces associated with the upstroke and downstroke. We interpret the difference in average ridge angle between the primary and secondary diaphyseal ridges in *Arambourgiania* to indicate that this individual was not solely gliding (non-powered flight where gravity is the energy source) but was soaring (sustained powered flight that requires launch and maintenance flapping). This evidence, combined with the stratigraphic evidence that *Arambourgiania* existed in a marine environment, highlights an interesting dichotomy for giant pterosaurs, which are otherwise known from terrestrial deposits. Our findings suggest that some giant azhdarchids were volant, perhaps supported by marine thermal soaring given the geological context of their fossils.

←FIGURE 14. Comparison of the internal structure of pterosaur and bird wing bones. **A**, photograph of the bone structure visible on the surface of the left humerus of *Inabtanin alarabia*. **B**, photograph of the bone structure visible on the exposed surface of the humerus of *Arambourgiania philadelphiae*. **C**, μCT slice from the midshaft of the humerus of *Inabtanin alarabia*. **D**, μCT slice from the midshaft of the humerus of *Arambourgiania philadelphiae*. **E**, three-dimensional reconstruction of the humerus of *Inabtanin alarabia* displaying struts. **F**, three-dimensional reconstruction of the humerus of *Arambourgiania philadelphiae* displaying helical ridges. **G**, photograph of the cross-sectional anatomy of the humerus of a cape vulture. The humeral midshaft contains struts hypothesized to resist bending forces during flight (modified from Sullivan et al., 2017). **H**, photograph of the cross-sectional anatomy of the ulna of a turkey vulture. The humeral midshaft contains helical ridges hypothesized to resist torsional forces during soaring (modified from Sullivan et al., 2017). Scale bars equal 5 mm.

The correlations presented here are supported by comparing the anatomy of individual birds and pterosaurs to materials science analyses (Kiang, 2013; Novitskaya et al., 2017; Sullivan et al., 2017). We seek to establish a more thorough understanding of the link between internal structure and flight behavior in modern and extinct Aves as well as pterosaur fossils. This research supports the pursuit of questions about the links of body mass, and wing morphology (wingspan, aspect ratio, wing loading) with flight capacity and flight style.

CONCLUSION

The remains of *Inabtanin* and *Arambourgiania* are remarkable for their three-dimensional preservation and for *Inabtanin* being one of the most complete individual pterosaurs to be recovered from Afro-Arabia. These fossils provide us with an opportunity to establish the detailed anatomy of azhdarchoid pterosaurs in the Late Cretaceous. Internal bone structure of the humerus indicates that the wings of giant pterosaurs experienced mechanical loadings comparable to those experienced by modern volant birds. Additionally, this study provides a framework for further investigation of the correlation between internal bone structure and flight capacity and behavior, which has been observed on a case study basis but remains to be established as a biological principle associated with the mechanics of vertebrate flight.

DISCLOSURE STATEMENT

No potential conflict of interest was reported by the author(s).

ACKNOWLEDGMENTS

We are grateful to A. Sawarieh (Natural Resources Authority, Jordan) and J. Nazzal (Yarmouk University, Jordan), A. Jamman, J. Head, and M. Wilson for field assistance and A. Khammash (Pella Museum) for logistical and technical support. We also thank W. Sanders for preparation of the fossils; A. Rountrey, K. Grosh, and M. Wood for photogrammetry; C. Abraczinskas for artistic input; M. Friedman. J. El Adli, and K. Matsunaga for assistance with µCT scanning; M. Perez, and S. Kaneko for segmenting µCT scans. We are grateful for feedback from reviewers R. Pêgas and C. Palmer, which improved this manuscript. And finally, we are grateful to the UMMNH for providing a cast of the *Q. northropi* humerus and to M. Brown and C. Sagebiel at the University of Texas Austin VPL for access to Texas pterosaur specimens. The American Chemical Society Petroleum Research Fund (PRF 46006-E8 to JAWM) supported this fieldwork, and the Scott Turner Award (to KLR) supported this research.

AUTHOR CONTRIBUTIONS

KLR and JAWM designed the project and KLR drafted the manuscript. JAWM, ISAZ, MGA, HAA, AAS, and HAM performed the fieldwork. KLR and DMG gathered and analyzed the µCT data. All authors edited the manuscript.

DATA AVAILABILITY STATEMENT

The data that support the findings of this study are openly available at the University of Michigan Deep Blue Data site (https://doi.org/10.7302/c1fs-xb12).

ORCID

Iyad S. A. Zalmout http://orcid.org/0000-0003-1874-801X
Jeffrey A. Wilson Mantilla http://orcid.org/0000-0003-2469-7028

LITERATURE CITED

Alexander, R. M. (1998). All-time giants: the largest animals and their problems. *Palaeontology*, *41*(6), 1231–1245.
Andres, B., & Langston, W. (2021). Morphology and taxonomy of *Quetzalcoatlus* Lawson 1975 (Pterodactyloidea: Azhdarchoidea). *Journal of Vertebrate Paleontology*, *41*(sup1), 46–202. doi:10.1080/02724634.2021.1907587
Arambourg, C. (1959). *Titanopteryx philadelphiae* nov. gen., nov. sp., pterosaurien geant. *Notes et Mémoires du Moyen Orient*, *7*, 229–234.
Averianov, A. O. (2010). The osteology of *Azharcho lancicollis* Nessov, 1984 (Pterosauria, Azhdarchidae) from the Late Cretacous of Uzbekistan. *Proceedings of the Zoological Institute RAS*, *314*(3), 264–317. doi:10.31610/trudyzin/2010.314.3.264
Bakhvalov, Y. O., Petrokovskiy, SA, Polynovskiy, V. P., & Razin, A. F. (2009). *Composite irregular lattice shells designing for space applications.* 17th International Conference on Composite Materials, Edinburgh, Scotland.
Bardet, N., & Suberbiola, X. P. (2002). Marine reptiles from the Late Cretaceous phosphates of Jordan: palaeobiogeographical implications. *Geodiversitas*, *24*(4), 831–839.
Bennett, S. C. (1993). The ontogeny of *Pteranodon* and other pterosaurs. *Paleobiology*, *19*(1), 92–106. doi:10.1017/S0094837300012331
Bonde, N., & Christiansen, P. (2003). The detailed anatomy of *Rhamphorhynchus*: axial pneumaticity and its implications. *Geological Society, London, Special Publications*, *217*(1), 217–232. doi:10.1144/GSL.SP.2003.217.01.13
Britt, B. B. (1993). Pneumatic postcranial bones in dinosaurs and other archosaurs [unpublished Ph.D. thesis]. University of Calgary.
Buffetaut, E., Grigorescu, D., & Csiki, Z. (2002). A new giant pterosaur with a robust skull from the latest Cretaceous of Romania. *Naturwissenschaften*, *89*(4), 180–184. doi:10.1007/s00114-002-0307-1
Buffetaut, E., Grigorescu, D., & Csiki, Z. (2003). Giant azhdarchid pterosaurs from the terminal Cretaceous of Transylvania (western Romania). *Geological Society, London, Special Publications*, *217*(1), 91–104. doi:10.1144/GSL.SP.2003.217.01.09
Butler, R. J., Barrett, P. M., & Gower, D. J. (2009). Postcranial skeletal pneumaticity and air-sacs in the earliest pterosaurs. *Biology Letters*, *5*(4), 557–60. doi:10.1098/rsbl.2009.0139
Chatterjee, S., & Templin, R. J. (2004). Posture, locomotion, and paleoecology of pterosaurs. *Geological Society of America, Special Paper*, *376*, 1–64.
Claessens, L. P. A. M., O'Connor, P. M., & Unwin, D. M. (2009). Respiratory evolution facilitated the origin of pterosaur flight and aerial gigantism. *PLoS ONE*, *4*(2), e4497. doi:10.1371/journal.pone.0004497
Frey, E., & Martill, D. M. (1996). A reappraisal of *Arambourgiania* (Pterosauria, Pterodactyloidea): one of the world's largest flying animals. *Neues Jahrbuch für Geologie und Paläontologie - Abhandlungen*, *199*(2), 221–247. doi:10.1127/njgpa/199/1996/221
Frost, H. M. (1960a). *The Utah Paradigm of Skeletal Physiology Vol. 1*. ISMNI.
Frost, H. M. (1960b). *The Utah Paradigm of Skeletal Physiology Vol. 2*. ISMNI.
Geist, N. R., Hillenius, W. J., Frey, E., Jones, T. D., & Elgin, R. A. (2014). Breathing in a box: constraints on lung ventilation in giant pterosaurs. *The Anatomical Record*, *297*(12), 2233–2253. doi:10.1002/ar.22839
Giffin, E. B. (1990). Gross spinal anatomy and limb use in living and fossil reptiles. *Paleobiology*, *16*(4), 448–458. doi:10.1017/S0094837300010186
Henderson, D. M. (2010). Pterosaur body mass estimates from three-dimensional mathematical slicing. *Journal of Vertebrate Paleontology*, *30*(3), 768–785. doi:10.1080/02724631003758334
Kaddumi, H. F. (2009). *Fossils of the Harrana Fauna and the Adjacent Areas.* Contributions from the Eternal River Museum of Natural History.
Kaup, J. J. (1834). Versuch einer Eintheilung der Säugethiere in 6 Stämme und der Amphibien in 6 Ordnungen. *Isis*, *3*, 311–315.
Kiang, J. (2013). Avian wing bones [Unpublished Master of Science Thesis]. University of California, San Diego.
Martill, D. M., Frey, E. & Sadaqah, R. M. (1996). The first dinosaur from the Hashemite Kingdom of Jordan. *Neues Jahrbuch für Geologie und Paläontologie - Monatshefte, 1996*(3), 147–154. doi:10.1127/njgpm/1996/1996/147

Martill, D. M., & Moser, M. (2017). Topotype specimens probably attributable to the giant azhdarchid pterosaur *Arambourgiania philadelphiae* (Arambourg 1959). In D. W. E. Hone, M. P. Witton, & D. M. Martill (Eds.), *New Perspectives on Pterosaur Palaeobiology, Geological Society Special Publication, 455* (pp. 159–169.

Martin, E. G., & Palmer, C. (2014a). Air space proportion in pterosaur limb bones using computed tomography and its implications for previous estimates of pneumaticity. *PLoS ONE*, *9*(5), 1–7.

Martin, E. G., & Palmer, C. (2014b). A novel method of estimating pterosaur skeletal mass using computed tomography scans. *Journal of Vertebrate Paleontology*, *34*(6), 1466–1469. doi:10.1080/02724634.2014.859621

Middleton, K. M., & English, L. T. (2015). Challenges and advances in the study of pterosaur flight. *Canadian Journal of Zoology*, *93*(12), 945–959. doi:10.1139/cjz-2013-0219

Naish, D., & Witton, M. P. (2017). Neck biomechanics indicate that giant Transylvanian azhdarchid pterosaurs were short-necked arch predators. *PeerJ*, *5*, e2908. doi:10.7717/peerj.2908

Naish, D., Witton, M. P., & Martin-Silverstone, E. (2021). Powered flight in hatchling pterosaurs: evidence from wing form and bone strength. *Scientific Reports*, *11*(1), 13130. doi:10.1038/s41598-021-92499-z

Nesov, L. A. (1984). [Pterosaurs and birds of the Late Cretaceous of Central Asia.] *Paleontologischeskii Zhurnal* 1984(1), 47–57. [In Russian].

Nesov, L. A., Kanznyshkina, L. F., & Cherepanov, G. O. (1987). Dinosaurs, crocodiles and other archosaurs from the Late Mesozoic of central Asia and their place in ecosystems. In *Abstracts of the 33rd session of the All-Union Palaeontological Society* (pp. 46–47.

Novitskaya, E., Ruestes, C. J., Porter, M. M., Lubarda, V. A., Meyers, M. A., & McKittrick, J. (2017). Reinforcements in avian wing bones: experiments, analysis, and modeling. *Journal of the Mechanical Behavior of Biomedical Materials*, *76*(2017), 85–96. doi:10.1016/j.jmbbm.2017.07.020

Pennycuick, C. J. (1982). The flight of petrels and albatrosses (Procellariiformes), observed in south Georgia and its vicinity. *Philosophical Transactions of the Royal Society of London, Series B, Biological Sciences*, *300*(1098), 75–106.

Pennycuick, C. J. (2008). *Modeling the Flying Bird*. Elseview Academic Press.

Plieninger, F. (1901). Beitrage zur Kenntnis das Flugsaurier. *Palaeontographica*, *48*, 65–90.

Powell, J. H. (1989). Stratigraphy and sedimentation of the Phanerozoic rocks in central and south Jordan. Part B: Kurnub, Ajlun and Belqa groups. *Natural Resources Authority Geological Bulletin*, *11*, 1–130.

Proctor, N. S., & Lynch, P. J. (1993). *Manual of Ornithology: Avian Structure and Function*. Yale University Press.

Salem, B. S. (2023). Geological and paleontological studies on new pterosaur and crocodyliform fossils from the Upper Cretaceous (Cenomanian) Bahariya Formation, Bahariya Oasis, Egypt [Unpublished Master of Science Thesis]. Ohio University.

Sato, K., Sakamoto, K. Q., Watanuki, Y., Takahashi, A., Katsumata, N., Bost, C. A., & Weimerskirch, H. (2009). Scaling of soaring seabirds and implications for flight abilities of giant pterosaurs. *PLoS ONE*, *4*(4), 1–6. doi:10.1371/journal.pone.0005361

Sullivan, T. N., Wang, B., Espinosa, H. D., & Meyers, M. A. (2017). Extreme lightweight structures: avian feathers and bones. *Materials Today*, *20*(7), 377–391. doi:10.1016/j.mattod.2017.02.004

Tschopp, E. (2016). Nomenclature of vertebral laminae in lizards, with comments on ontogenetic and serial variation in lacertini (Squamata, Lacertidae). *PLoS ONE*, *11*(2), 1–21. doi:10.1371/journal.pone.0149445

Vila Nova, B. C., Sayaõ, J. M., Langer, M. C., & Kellner, A. W. A. (2015). Comments on the cervical vertebrae of the Tapejaridae (Pterosauria, Pterodactyloidea) with description of new specimens. *Historical Biology*, *27*(6), 771–781. doi:10.1080/08912963.2015.1007049

Wilson, J. A. (2006). Anatomical nomenclature of fossil vertebrates: standardized terms or lingua franca? *Journal of Vertebrate Paleontology*, *26*(3), 511–518. doi:10.1671/0272-4634(2006)26[511:ANOFVS]2.0.CO;2

Witton, M. P. (2007). Titans of the skies: azhdarchid pterosaurs. *Geology Today*, *23*(1), 33–38. doi:10.1111/j.1365-2451.2007.00596.x

Witton, M. P. (2008). A new approach to determining pterosaur body mass and its implications for pterosaur flight. In D. W. E. Hone and E. Buffetaut (Eds.) *Flugsaurier: Pterosaur Papers in Honour of Peter Wellnhofer, Zitteliana, B28*, 143–158.

Witton, M. P., & Habib, M. B. (2010). On the size and flight diversity of giant pterosaurs, the use of birds as pterosaur analogues and comments on pterosaur flightlessness. *PLoS ONE*, *5*(11), e13982. doi:10.1371/journal.pone.0013982

Witton, M. P., & Naish, D. (2008). A reappraisal of azhdarchid pterosaur functional morphology and paleoecology. *PLoS ONE*, *3*(5), 17–32. doi:10.1371/journal.pone.0002271

Wolff, J. (1986). *The Law of Bone Remodeling*. Berlin Heidelberg New York: Springer (translation of the German 1892 edition).

Zalmout, I. S., & Mustafa, H. (2001). A selachian fauna from the Late Cretaceous of Jordan. *Abhath Al-Yarmouk: Basic Sciences and Engineering*, *10*(2b), 377–434.

Handling Editor: Elizabeth Martin-Silverstone.